Streamwise confinement effects in a temporally developing stably stratified shear layer

Takumi Akao (赤尾 拓海), Tomoaki Watanabe (渡邉 智昭),[a] and Koji Nagata (長田 孝二)

Department of Mechanical Engineering and Science, Kyoto University, Kyoto 615-8530, Japan

(Dated: 15 July 2025)

Direct numerical simulations are conducted to investigate the large-scale features of a stably stratified shear layer. The fully-developed turbulent shear layer exhibits two distinct large-scale structures: one is a typical large-scale structure (LSS) with a scale proportional to the shear layer thickness, and the other is an elongated large-scale structure (ELSS) with a streamwise length much greater than that of the LSS. Simulations employ computational domains with varying streamwise lengths. Autocorrelation functions of velocity reveal that the ELSS meanders in the horizontal plane. This meandering is altered in smaller domains, where confinement effects eventually suppress ELSS growth. Comparisons across domain sizes highlight the role of the ELSS in flow evolution. The mean and root-mean-square fluctuations of velocity and density remain unaffected by the growth of the ELSS. The LSS length scale consistently scales with the shear layer thickness and is not influenced by the ELSS. The behavior of the dissipation coefficient indicates that energy transfer from large to small scales is predominantly driven by the LSS rather than the ELSS. Counter-gradient diffusion of momentum and density is known to occur at scales between the LSS and ELSS; this feature is shown to be linked to the development of the ELSS. The results indicate that the ELSS has minimal influence on flow properties at scales smaller than the LSS, which govern the averages and variances of velocity and density, while it plays a significant role at scales larger than the LSS.

[a] Author to whom correspondence should be addressed: watanabe.tomoaki.8x@kyoto-u.ac.jp

I. INTRODUCTION

Turbulence in a stably stratified fluid is commonly observed in the ocean and atmosphere.[1–3] One important mechanism of turbulence generation in natural environments is instability arising from shear currents.[4] Shear can lead to the Kelvin–Helmholtz (KH) instability, which induces intense turbulent motions and enhances the transport of momentum and scalars in the flow.[5,6] The process of turbulence generation via KH instability under stable stratification has received significant attention in previous studies. A representative laboratory example is the formation of a stably stratified shear layer between two parallel flows with different velocities and densities.[7,8] This flow configuration has also been examined using direct numerical simulations and large-eddy simulations.[9,10] It has been reported that the vertical density profiles of stably stratified shear layers resemble those observed in turbulent patches in the oceanic thermocline.[9] At high Prandtl numbers, the density interface can become thinner than the shear layer, giving rise to Holmboe instability, which also leads to turbulence generation.[11,12] Turbulent shear layers driven by Holmboe instability have been investigated through both experiments and numerical simulations.[12–18] In contrast, the present study focuses on turbulence generated by KH instability.

Several studies have focused on the transition process triggered by KH instability. The KH instability initially generates large-scale roller vortices aligned in the spanwise direction. Subsequently, depending on the flow conditions, various types of secondary instabilities or vortex interactions occur following the formation of the primary vortices, leading to the development of three-dimensional turbulence.[19–22]In the absence of stable stratification, turbulence in a shear layer is maintained by the production mechanism associated with the mean shear.[23,24] In contrast, buoyancy forces in a stably stratified fluid suppress vertical turbulent motions and promote decay of the turbulent shear layer. This decay process has been analyzed using the budget equations of turbulent kinetic energy and potential energy.[10,25] Other studies have quantified parameters characterizing turbulent mixing, such as mixing efficiency and the turbulent Prandtl number,[26–30] which are essential for modeling mixing processes in geophysical flows.

Turbulence is often investigated in terms of coherent structures, which are defined by characteristic patterns in flow variables. For example, vortices are commonly described as tubular regions of fluid exhibiting intense rotational motion.[31] Flow visualizations from numerical simulations have shown that vortices in stably stratified shear layers frequently have a hairpin shape.[32–35] These hairpin vortices induce velocity fluctuations that contribute to vertical turbulent transport. Such vortical structures are typically identified using quantities based on velocity gradients and reflect the small-scale features of turbulence. In contrast, large-scale flow structures are often identified using velocity or pressure fields.[36,37]

Both small- and large-scale structures play important roles in turbulence. Small-scale structures are primarily responsible for the dissipation of turbulent kinetic energy and for irreversible density mixing through molecular or thermal diffusion. In contrast, momentum and density transport by stirring motions predominantly occurs at large scales. In stably stratified shear layers, a characteristic length scale for large-scale motions is the shear layer thickness. When turbulence develops from KH instability, the shear layer thickness defines the typical large-scale structures (LSS), such as roller vortices that remain from the instability.[38–40] As the turbulent shear layer evolves in a stably stratified fluid, structures with much larger scales than the LSS can emerge.[25] These very-large-scale structures exhibit strong anisotropy, with their streamwise length significantly exceeding their spanwise and vertical scales. They are referred to as elongated large-scale structures (ELSS) and are evident in the distribution of positive and negative streamwise velocity fluctuations that are elongated in the streamwise direction. Similar elongated structures are also observed in wall-bounded shear flows.[41] The ELSS in stably stratified shear layers develop due to enhanced mean shear effects under stable stratification, emerging when the mean shear time scale becomes much shorter than the large-eddy turnover time.[42] Both LSS and ELSS carry significant turbulent kinetic energy and contribute to density fluctuations. The decomposition of velocity fields into LSS and ELSS scales using a low-pass filter suggests that the ELSS contains approximately 50% of the turbulent kinetic energy.[25] In addition, a proper orthogonal decomposition (POD) analysis has shown that the ELSS can be well reconstructed using the first several POD modes that together capture 50% of the turbulent kinetic energy.[42] These results suggest that the ELSS carry a substantial fraction of the kinetic energy in the flow. When the ELSS becomes sufficiently developed, the one-dimensional kinetic energy spectrum evaluated with streamwise wavenumber k_x follows a k_x^{-1} power law between the LSS and ELSS scales.[25] This k_x^{-1} law has also been observed in numerical simulations modeling KH instability events in polar mesospheric clouds,[6,22] suggesting that ELSS may influence the characteristics of atmospheric turbulence.

The role of ELSS in the evolution of stably stratified shear layers remains incompletely understood, although previous studies have revealed their presence and generation mechanisms. The present study conducts new direct numerical simulations (DNS) of stably stratified shear layers to examine how the ELSS influence flow evolution. Several approaches are available to investigate how turbulent structures affect flow evolution. One approach is to eliminate or modulate specific turbulent structures to assess how their absence alters the flow evolution. Using this method, the origin of large-scale roller vortices in turbulent wakes was studied by suppressing Kármán vortices with porous structures.[43] The role of internal shear instability in small-scale turbulence was also studied using this approach.[44–46] Artificial velocity perturbations that trigger small-scale shear instability were superimposed on decaying turbulence to evaluate the effects of the instability. Similarly, the role of large-scale motions in wall turbulence was investigated through simulations employing small computational domains.[47] In such cases, small domains inhibit the growth of large-scale structures, and comparisons between different domain sizes reveal how the presence of large-scale structures influences small- to moderate-scale turbulent motions. The present study adopts this approach to explore the role of ELSS in temporally evolving stably stratified shear layers. Specifically, DNS is performed using various streamwise domain sizes. As the streamwise size decreases, ELSS development is inhibited by confinement effects. Comparisons among simulations with different domain sizes are used to elucidate how ELSS influence the evolution of the flow.

The numerical setup is described in § II. Section III presents the results of the DNS, including one- and two-point statistics of velocity and density, as well as spectral analyses. Additionally, the correlation analysis reveals the spatial organization of the ELSS, which has not been previously discussed. These statistics are also used to evaluate several key parameters relevant to modeling stably stratified shear flows, in order to relate the development of ELSS to turbulence dynamics and the mixing process. Finally, the paper is summarized in § IV.

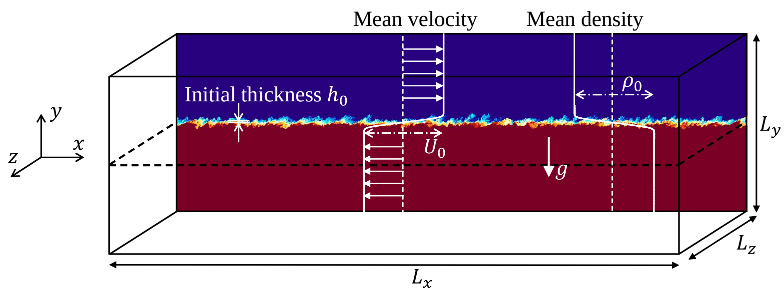

FIG. 1. Computational domain and mean streamwise velocity and density profiles of a stably stratified shear layer.

II. DIRECT NUMERICAL SIMULATION OF A STABLY STRATIFIED SHEAR LAYER

A. DNS of a stably stratified shear layer

The present study performs DNS of a temporally evolving stably stratified shear layer within a domain that is periodic in the streamwise and spanwise directions. Figure 1 illustrates the numerical setup. The streamwise velocity and density vary within a thin layer, which becomes turbulent due to the KH instability. The differences in streamwise velocity and density between the upper and lower regions are denoted by U_0 and ρ_0, respectively. This flow configuration has been widely used in numerical studies of stably stratified turbulence.[9] The streamwise, vertical, and spanwise directions are denoted by x, y, and z, respectively, with corresponding velocity components u, v, and w. The density field is represented as $\rho_a + \rho(x, y, z, t)$, where ρ_a is a constant reference density and ρ is the deviation from ρ_a. The governing equations are the Navier–Stokes equations under the Boussinesq approximation and are expressed as follows:

$$\begin{aligned} \frac{\partial u_j}{\partial x_j} &= 0, \\ \frac{\partial u_i}{\partial t} + \frac{\partial u_i u_j}{\partial x_j} &= -\frac{1}{\rho_a}\frac{\partial p}{\partial x_i} + \nu \frac{\partial^2 u_i}{\partial x_j \partial x_j} - g\frac{\rho}{\rho_a}\delta_{i2}, \\ \frac{\partial \rho}{\partial t} + \frac{\partial u_j \rho}{\partial x_j} &= \kappa \frac{\partial^2 \rho}{\partial x_j \partial x_j}, \end{aligned} \tag{1}$$

where subscripts $i, j = 1, 2, 3$ correspond to the x, y, and z directions, respectively; t is time; p is pressure; ν is the kinematic viscosity; κ is the molecular diffusivity for density; and g is the gravitational acceleration. The gravitational force acts in the vertical direction and is represented using the Kronecker delta δ_{ij}.

The flow is statistically homogeneous in the x and z directions, where periodic boundary conditions are applied. Free-slip boundary conditions are imposed on the upper and lower boundaries in the vertical (y) direction. Statistical quantities are defined using spatial averages $\langle f \rangle$ taken over horizontal planes as functions of time and y. The fluctuating component is defined as $f' = f - \langle f \rangle$. The initial mean streamwise velocity is specified as $\langle u \rangle = 0.5U_0 \tanh(2y/h_0)$, where h_0 denotes the initial shear layer thickness. The initial mean velocities in the vertical and spanwise directions are set to zero. The initial velocity field is constructed by superimposing velocity fluctuations onto the mean velocity as $(u, v, w) = (\langle u \rangle + u', v', w')$. The initial density field is given by $\rho = -0.5\rho_0 \tanh(2y/h_0)$ without any fluctuations. The initial velocity fluctuations are generated using spatially correlated random numbers,[48] as follows. A characteristic length scale $L_f = 0.34h_0$ and root-mean-square (rms) velocity u_f are specified, where $u_f = 0.025U_0$ for $|y|/h_0 < 0.7$ and zero elsewhere. First, a coarse auxiliary grid with resolution $\Delta_f = L_f$ is constructed, and uniform random numbers in the range $[-1, 1]$ are assigned independently to each of the three velocity components at every point on this grid. These random fields are then interpolated onto the fine DNS grid using trilinear interpolation. Next, on each x–z plane, the interpolated velocity fields are normalized to have zero mean and a root-mean-square (rms) value of u_f, where the statistics of the random velocity are defined using spatial averages in the x–z plane. The resulting random velocity field is used as the initial fluctuations. The energy spectra of the generated fluctuations have been examined in prior studies,[25,48] confirming that the velocity fields exhibit an energy-containing scale of L_f and the target rms value u_f.

The flow is characterized by three non-dimensional parameters: the Reynolds number $Re = U_0 h_0/\nu$, the Prandtl number $Pr = \nu/\kappa$, and the Richardson number $Ri = g\rho_0 h_0/(\rho_a U_0^2)$. Previous studies have examined the dependence of flow characteristics on these parameters.[9,20,21,25,29] The present study focuses on the development of ELSS, which emerge when $Ri > 0.06$ and Re is sufficiently high for the initial shear layer to develop into turbulence.[25,35] These prior investigations have shown that the large-scale flow features associated with ELSS are largely insensitive to variations in (Re, Ri). A LES study has confirmed the ELSS development at $Re = 40000$ similarly to low Re cases.[25,35] The dependence on Pr has also been studied in Ref. 29, which reported that the temporal evolution of velocity statistics remains similar for Pr values between 1 and 16. Based on these findings, the present study adopts $Re = 600$, 1200, and 1800, with fixed parameters $(Ri, Pr) = (0.06, 1)$. Different parameter sets would yield qualitatively similar results, provided that (Re, Ri) satisfy the conditions necessary for the growth of ELSS, as supported by previous comparisons of velocity and density statistics across a range of parameters.

The present study focuses on $Pr = 1$, and does note explore the Pr effects, which are important especially in small-scale density fluctuations and their coupling with the velocity field. Understanding this issue requires DNS with different Pr values, as in previous DNS studies on this issue.[12,15–17] The present study focuses on the ELSS, whose development is driven by mean shear rather than direct buoyancy effects.[42] In turbulent shear layers without density stratification, the shear layer thickness grows over time. Stratification suppresses this growth, thereby sustaining the mean velocity gradient. The enhanced mean shear resulting from this suppression promotes the growth of ELSS, consistent with mechanisms of anistropic structure growth due to strong mean shear predicted by rapid distortion theory.[49] In this process, the role of buoyancy is indirect, mainly through the modification of the shear profile, while direct buoyancy effects such as kinetic-to-potential energy conversion are less relevant. For this reason, a non-stratified shear layer also allows the growth of ELSS when the vertical layer development is inhibited by walls, while the ELSS does not appear in a freely evolving shear layer, where mean shear becomes weak with time.[42] This understanding has guided our focus on the velocity field and the use of $Pr = 1$. It is also worth noting that ELSS have been reported for turbulent shear layers arising from KH instability. As Pr increases, the initial shear layer has a thinner density interface, and Holmboe instabilities become dominant in the turbulent transition.[11,12] The existence of ELSS in turbulent flows triggered by Holmboe waves at high Pr remains unclear. Given that ELSS development is attributed to enhanced shear, ELSS is expected to emerge in Holmboe-wave-induced turbulent shear layers. However, verifying this hypothesis with numerical simulations would require DNS with very large domains and high spatial resolution, which become computationally prohibitive at high Prandtl numbers. Existing DNS studies with high Pr are generally restricted to relatively small computational domains, making it difficult to resolve ELSS development under such conditions.[12,15–18]

TABLE I. Parameters of DNS: the Reynolds number Re, the Richardson number Ri, the Prandtl number Pr, the domain size (L_x, L_y, L_z), the number of grid points (N_x, N_y, N_z), the time increment Δt, and the grid size $(\Delta_x, \Delta_y, \Delta_z)$. Here, Δ_y is evaluated at the shear layer center.

Case	Re	Ri	Pr	L_x/h_0	L_y/h_0	L_z/h_0	N_x	N_y	N_z	$\Delta t/t_r$	Δ_x/h_0	Δ_y/h_0	Δ_z/h_0
Re06Lx28	600	0.6	1	28	80	84	324	416	972	0.015	0.087	0.093	0.087
Re06Lx448	600	0.6	1	448	80	84	5184	416	972	0.015	0.087	0.093	0.087
Re12Lx28	1200	0.6	1	28	80	84	486	700	1458	0.01	0.058	0.055	0.058
Re12Lx56	1200	0.6	1	56	80	84	972	700	1458	0.01	0.058	0.055	0.058
Re12Lx112	1200	0.6	1	112	80	84	1944	700	1458	0.01	0.058	0.055	0.058
Re12Lx448	1200	0.6	1	448	80	84	7776	700	1458	0.01	0.058	0.055	0.058
Re18Lx28	1800	0.6	1	28	80	84	648	948	1944	0.0075	0.044	0.041	0.044
Re18Lx448	1800	0.6	1	448	80	84	10368	948	1944	0.0075	0.044	0.041	0.044

B. Numerical methods and parameters

The governing equations are solved using an in-house DNS code based on a fractional step method with finite difference schemes. This code is identical to that used in our previous studies,[35,45,50–52] where its validity was confirmed through comparisons with experimental and numerical results. Spatial derivatives are computed using fully conservative finite difference schemes: a fourth-order scheme in the horizontal directions and a second-order scheme in the vertical direction.[53] Time integration is performed using a third-order Runge–Kutta method. The Poisson equation for pressure is solved using the biconjugate gradient stabilized (Bi-CGSTAB) method.

Table I summerizes the computational parameters. The present study investigates how the emergence of ELSS alters the statistical behavior of the flow. To this end, DNS is performed with different streamwise domain sizes: $L_x = 28h_0$, $56h_0$, $112h_0$, and $448h_0$ for $Re = 1200$; $L_x = 28h_0$ and $448h_0$ for $Re = 600$ and 1800. Since ELSS are characterized by a large streamwise length scale, their development is inhibited when L_x is not sufficiently large, due to confinement effects. Comparing these cases helps to reveal how ELSS influence flow evolution. The domain sizes in the other directions are fixed across all cases at $(L_y, L_z) = (80h_0, 84h_0)$. The vertical domain size L_y is much larger than the thickness of the fully developed turbulent shear layer, which is approximately $10h_0$ in the present case. Therefore, the vertical boundaries do not affect the flow evolution. The spanwise domain size L_z is also chosen to ensure that the periodic boundary conditions in the z direction have minimal influence on the flow. Previous studies have examined confinement effects in the spanwise direction by conducting simulations with various values of L_z.[25,54,55] When L_z is too small, the three-dimensionality of roller vortices generated by the KH instability is suppressed. This confinement effect delays the generation of three-dimensional velocity fluctuations, because the interaction between neighboring roller vortices, that is facilitated by misalignment of their axes from the spanwise direction, is restricted under small L_z.[25,56] These previous findings suggest that $L_z = 84h_0$ in the present DNS is sufficiently large to ensure that the periodic boundary conditions in the spanwise direction have minimal influence.

The simulations are conducted up to $t = 320t_r$, where $t_r = h_0/U_0$ is the reference time scale of the shear layer. The computational domain is discretized using regular grids. The grid spacing is uniform in the x and z directions and non-uniform in the vertical (y) direction, where it becomes finer near the center of the shear layer ($y = 0$). The vertical grid refinement follows a hyperbolic tangent distribution, as described in Refs. 42 and 57. The numbers of grid points in the three directions are denoted by N_x, N_y, and N_z. Since the streamwise domain size varies across cases, N_x is adjusted accordingly. During the transitional regime, a thin interface of upper and lower fluids appear in braid regions, which are resolved with more than 10 grid points in one direction. The grid spacings are always smaller than twice the Kolmogorov length scale in the fully-developed three-dimensional turbulence regime after the transition, ensuring sufficient resolution to capture small-scale turbulent motions using the present central difference schemes, as confirmed by a grid dependence test.[57] The Kolmogorov scale is widely used in the literature as a characteristic measure of the smallest dynamically active scales in turbulence even when the flow is statistically ansisotropic and inhomogeneous. Many studies have shown that the diameters of vortex tubes and the thicknesses of vortex sheets scale with the Kolmogorov length in both homogeneous isotropic and inhomogeneous anisotropic flows such as jets, wakes, mixing layers, and boundary layers (Refs. 31, 58–63 for vortex tubes, Refs. 50, 64–66 for vortex sheets). Furthermore, one-dimensional energy spectra in these flows collapse at high wavenumbers when normalized by the Kolmogorov scale.[67] The radii of vortex tubes in stably stratified turbulent shear layers are approximately five times the Kolmogorov scale, in quantitative agreement with observations from non-stratified flows.[35] This consistency further supports the validity of using the Kolmogorov scale as a reference for characterizing the smallest scales of the turbulent shear layers after the transition.

For each value of L_x, the simulations are repeated N_S times using different initial velocity fluctuations. The values of N_S for $Re = 1200$ are 16, 8, 5, and 2 for $L_x/h_0 = 28$, 56, 112, and 448, respectively. For $Re = 600$ and 1800, N_S is 8 for $L_x/h_0 = 28$ and is 2 for $L_x/h_0 = 448$. Flow statistics are defined based on horizontal averages, with the number of available samples depending on L_x and L_z. As L_x decreases, fewer samples can be obtained from a single simulation. Therefore, a larger N_S is used for smaller L_x. All statistical quantities presented in this study are evaluated by taking ensemble averages over N_S simulations.

Three-dimensional profiles of flow variables are analyzed using statistics defined by averages over horizontal planes, evaluated as functions of height y and time. These statistics represent the flow state at each height and time. Some previous studies on stratified turbulent mixing have introduced diagnostic tools for examining bulk properties of the entire flow, based on vertical averaging and vertical density profiles.[26,68] However, when applied to regions near the outer edges of the shear layer, such methods can obscure the local characteristics of the ELSS, which develop only near the center of the shear layer.[25,35] Therefore, the present study adopts statistical analyses based on spatial averaging in the homogeneous directions, which more effectively capture the flow organization and dynamics associated with the ELSS.

III. RESULTS AND DISCUSSION

A. Instantaneous flow fields

The transition process from the initial laminar shear layer to turbulence is visualized in Figs. 2 and 3, which show two-dimensional density profiles in Re12Lx448. Each panel presents density distributions from $t/t_r = 30$ to 80 on both a vertical (x–y) plane at $z = 0$ and a horizontal (x–z) plane at the center of the shear layer ($y = 0$). For clarity, only a portion of the domain is shown in the x and y directions. The development of spanwise vortices due to the KH instability is observed in the x–y planes from $t/t_r = 30$ to 50, with characteristic vortex structures particularly evident at $t/t_r = 50$ in Fig. 2(c). These vortices

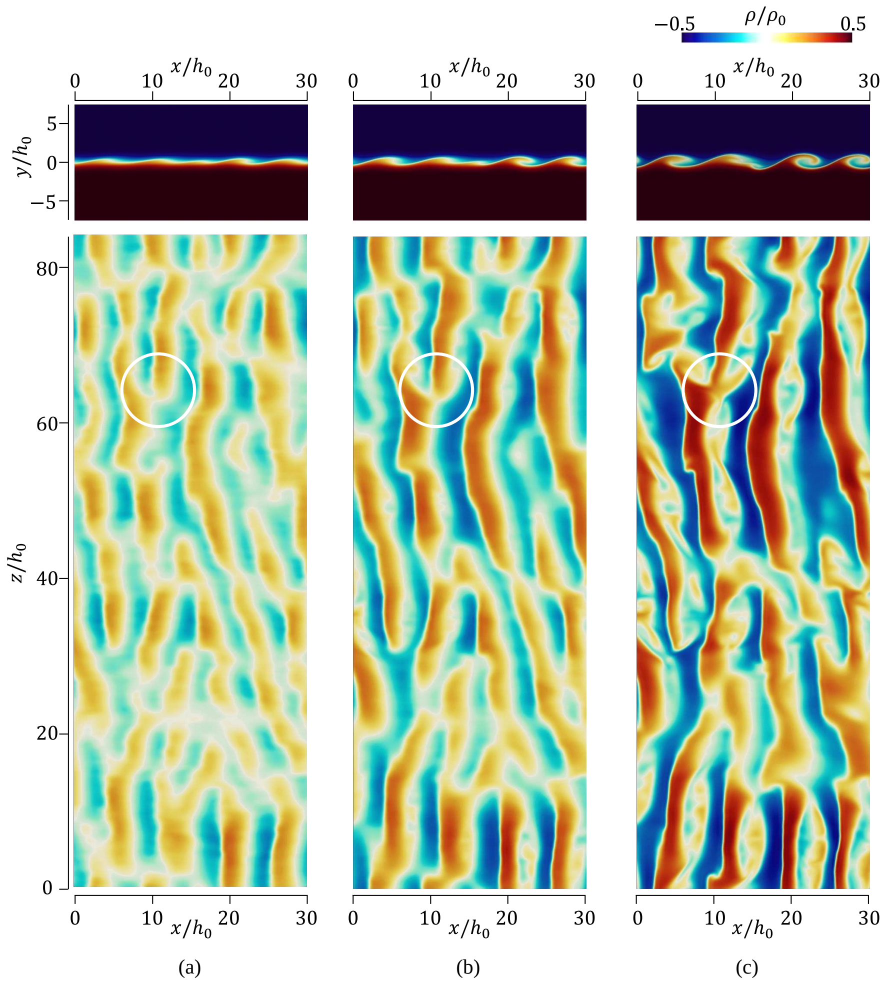

FIG. 2. Density profiles on the x–y plane at $z = 0$ and the x–z plane at the shear layer center ($y = 0$) in Re12Lx448: (a) $t/t_r = 30$; (b) $t/t_r = 40$; (c) $t/t_r = 50$.

produce alternating strip-like density patterns on the x–z plane. These patterns have a finite spanwise length and are slightly inclined with respect to the spanwise direction, indicating that the vortices are misaligned rather than perfectly spanwise. This misalignment promotes interactions between neighboring vortices, leading to their collapse and the generation of

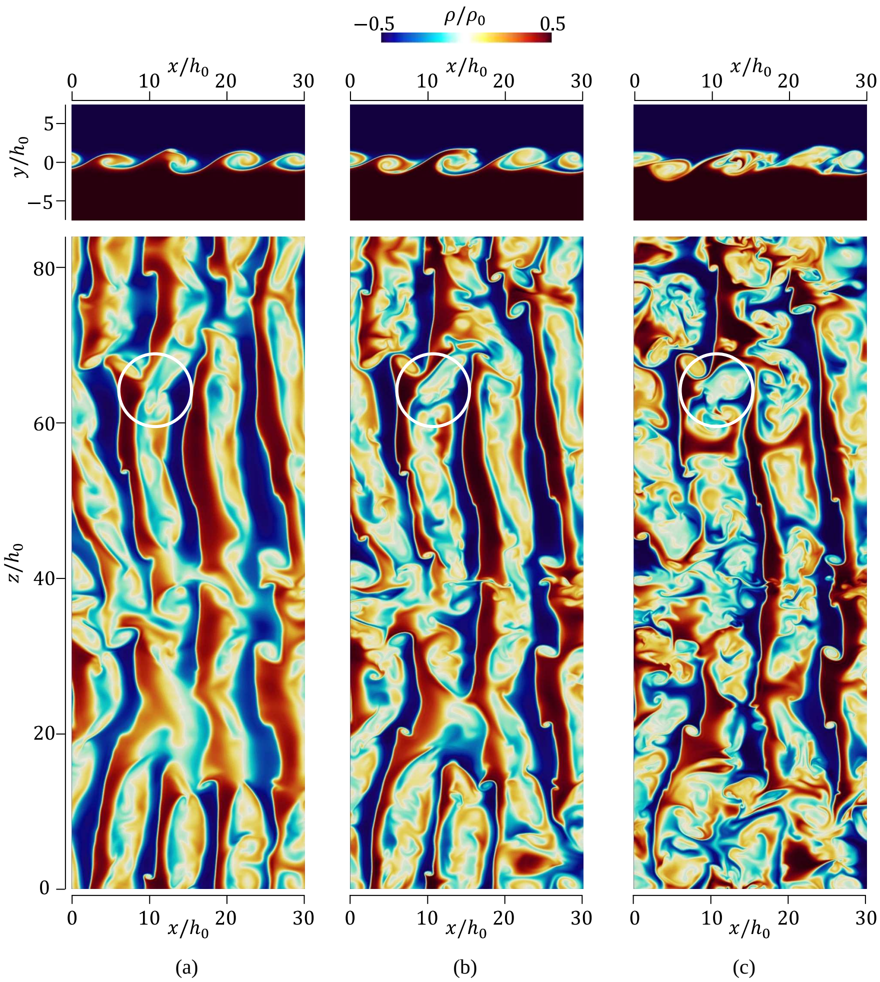

FIG. 3. The same as Fig. 2 but for (a) $t/t_r = 60$, (b) $t/t_r = 70$, and (c) $t/t_r = 80$.

small-scale density fluctuations, as seen from $t/t_r = 60$ to 80 in Fig. 3. One example of such an interaction is highlighted by white circles in Figs. 2 and 3. These interactions trigger the onset of fully three-dimensional turbulence. This transition mechanism via misaligned vortex interaction aligns with experimental and numerical observations of both stratified and non-stratified shear layers.[55,69–73] Similar mechanisms have been documented in atmospheric observations of KH instability,[4,74,75] as summarized in Refs. 22 and 76. Simulations with different Re and Ri have consistently observed the transition due to misaligned vortex interacton, and this mechanism seems ubiquitous in the KH instability.[77]

Each spanwise vortex arising from the KH instability is known to undergo secondary instabilities, such as convective instabilities in the vortex core and secondary KH instabilities in the braid region between vortices.[20,70] However, it has been shown that interactions between misaligned vortices result in a more rapid onset of intense turbulence than these secondary instabilities, and thus play a dominant role in the transition process.[22,77] The importance of domain size has been demonstrated in prior numerical studies of turbulent shear layers developing via KH instability.[25,54,55,77] In small spanwise domains, periodic boundary conditions force each vortex to reconnect with itself via the boundary, resulting in perfectly aligned vortices and suppressing their interaction. Under such confinement, the vortices remain nearly two-dimensional during the initial stage of the transition, exhibiting much weaker spanwise velocity fluctuations than in the streamwise and vertical directions.[25] In such cases, the transition to turbulence can be dominated by the secondary instabilities of each vortex typically observed in two-dimensional simulations and three-dimensional simulations with a small spanwise domain size.[9,20,21,78] This issue has also been pointed out in previous numerical simulations of stably stratified shear layers with varying spanwise domain sizes.[25,77] McMullan proposed a criterion to prevent spanwise confinement effects in simulations of spatially developing non-stratified shear layers.[55] The criterion requires the ratio of spanwise domain size L_z to the momentum thickness $I_u = \int_{-L_y/2}^{L_y/2}(1 - 4\langle u\rangle^2/U_0^2)\,dy$ to exceed 2.5. In the present DNS, this ratio satisfies $L_z/I_u > 20$ during the transition period ($t/t_r < 100$), thus meeting the criterion. Although this threshold was originally derived for spatially developing non-stratified flows, the significantly larger value in the present temporally evolving stratified case strongly suggests that confinement effects are negligible.

The instantaneous flow fields are compared for different domain sizes using Re12Lx28 and Re12Lx448, which represent cases with and without streamwise confinement effects, respectively. Figures 4, 5, and 6 illustrate the development of the turbulent shear layer, showing the streamwise velocity u on an x–y plane at various time instances. Figure 4 shows the entire streamwise extent of the Re12Lx28 domain, while Fig. 5 displays the full streamwise range for Re12Lx448. The white rectangle in Fig. 5 indicates the region visualized in Fig. 6. All figures show the vertical extent of $|y/h_0| \leq 10$, where the turbulent shear layer

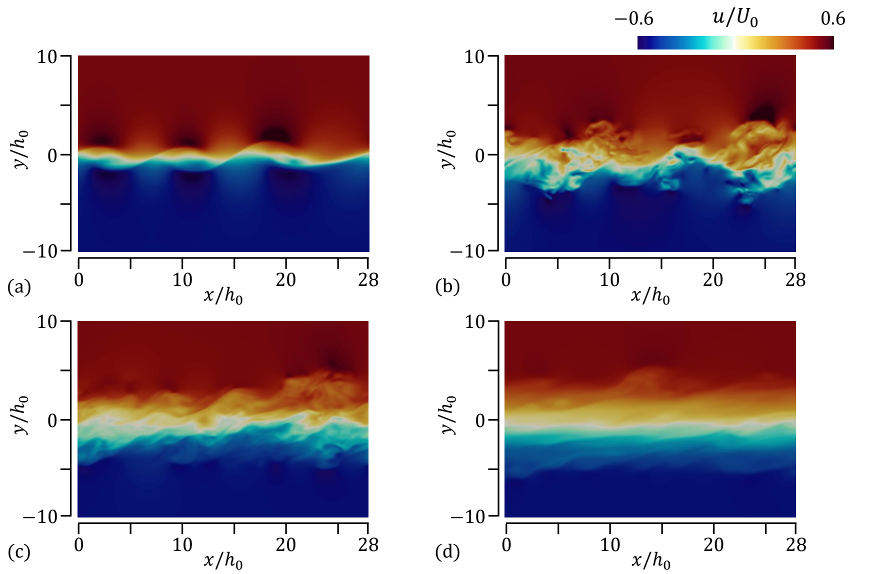

FIG. 4. Instantaneous streamwise velocity on an x–y plane in Re12Lx28 at (a) $t/t_r = 60$, (b) $t/t_r = 120$, (c) $t/t_r = 200$, and (d) $t/t_r = 320$. A part of the computational domain in the y direction is shown here.

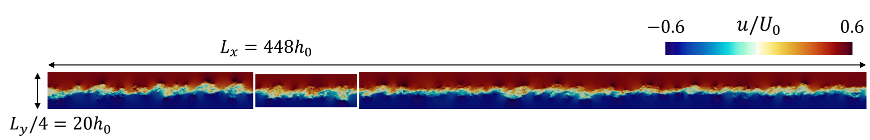

FIG. 5. Instantaneous streamwise velocity on an x–y plane in Re12Lx448 at $t/t_r = 120$. A part of the computational domain in the y direction is shown here.

develops. Multiple roller vortices generated by the KH instability are observed in the early stages of flow development, specifically at $t/t_r = 60$ in Figs. 4(a) and 6(a). These vortices grow and eventually collapse due to interactions with neighboring vortices. After the collapse of the vortices, three-dimensional turbulence develops within the shear layer, establishing a turbulent state around $t/t_r = 80$. Due to the suppressive effect of buoyancy on vertical turbulent diffusion, the vertical growth of the shear layer is limited. As a result, the shear

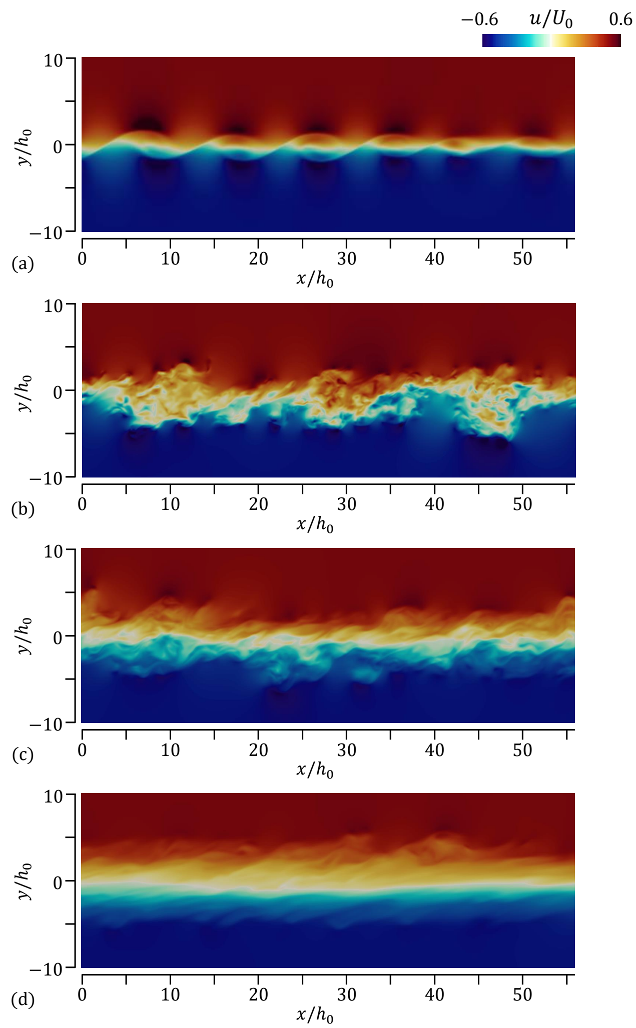

FIG. 6. Instantaneous streamwise velocity in the white box in Fig. 5 in Re12Lx448 at (a) $t/t_r = 60$, (b) $t/t_r = 120$, (c) $t/t_r = 200$, and (d) $t/t_r = 320$.

layer thickness, approximately corresponding to the region where $-0.5 \lesssim u/U_0 \lesssim 0.5$, shows little variation over the later period, from $t/t_r = 200$ to 320, as seen in Figs. 4(c, d) and 6(c, d). The visual patterns on the x–y plane are similar for both cases, indicating that streamwise

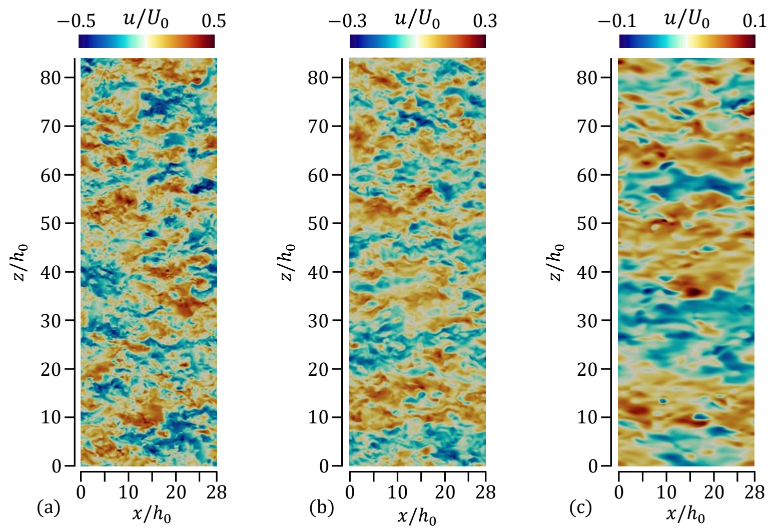

FIG. 7. Instantaneous streamwise velocity on the x–z plane at the shear layer center, $y = 0$, in Re12Lx28 at (a)$t/t_r = 120$, (b)$t/t_r = 200$, and (c)$t/t_r = 320$.

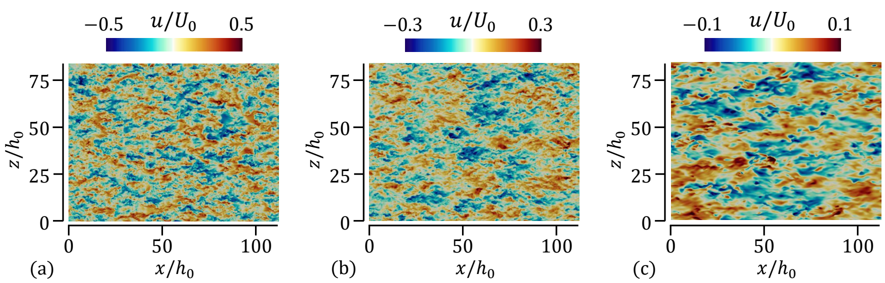

FIG. 8. The same as Fig. 7 but for Re12Lx112.

confinement effects in Re12Lx28 have minimal influence on the initial KH instability and the subsequent collapse of vortices.

Figures 7–9 present horizontal visualizations of the instantaneous streamwise velocity at the center of the shear layer for Re12Lx28, Re12Lx112, and Re12Lx448. Each figure shows the full horizontal domain. Unlike the x–y plane visualizations, the streamwise velocity dis-

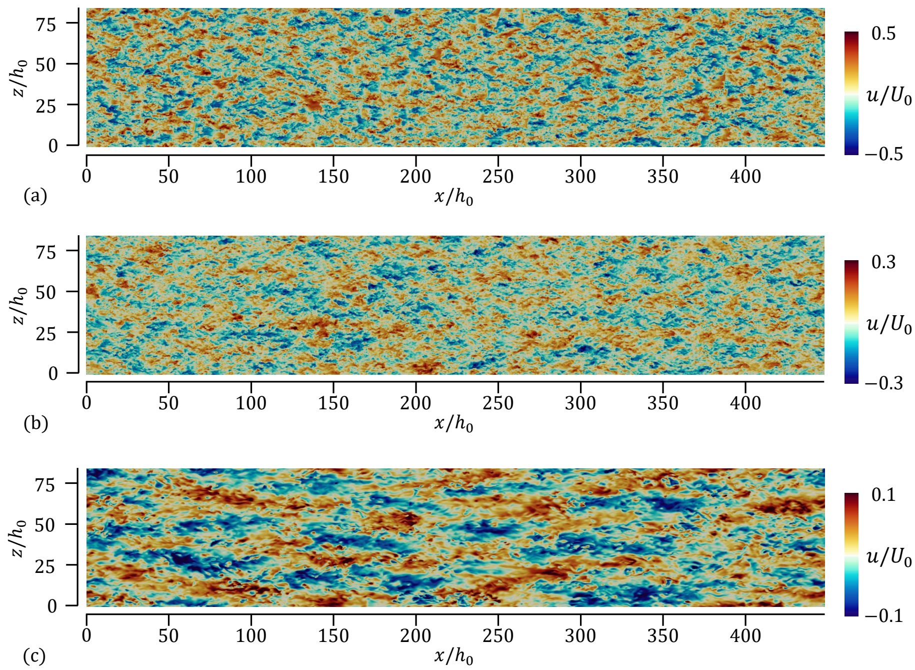

FIG. 9. The same as Fig. 7 but for Re12Lx448.

tributions on the horizontal plane exhibit noticeable differences across the different domain sizes. Large-scale flow structures can be identified from spatial velocity distributions. In turbulent shear layers, such structures are often visualized as alternating regions of positive and negative streamwise velocity.[35,79] In this study, regions with $u > 0$ and $u < 0$ are used for visual interpretation of large-scale features; however, this qualitative criterion is not employed in the statistical analyses that follow. As the flow evolves, the size of the regions with positive and negative u increases, indicating the development of larger-scale structures. In Re12Lx28 (Fig. 7), the streamwise extent of the structures eventually approaches the domain size L_x. At later times, especially around $t/t_r = 320$ in Fig. 7(c), the regions of positive and negative u span the entire domain and connect through the periodic boundaries at $x = 0$ and $x = 28h_0$. It is well known that periodic boundaries can introduce artificial effects when the characteristic scale of the flow structures exceeds half the computational domain size, as shown in the behavior of two-point correlation functions.[80] Once the size of the large-scale structures reaches the domain size L_x, these structures effectively become infinitely long due to the periodicity. This confinement effect becomes evident after $t/t_r = 200$ in Figs. 7(b, c).

Figures 8 and 9 show the instantaneous streamwise velocity field for Re12Lx112 and Re12Lx448. When the streamwise domain size is large, as in Re12Lx448, artificial effects from periodic boundaries do not influence the flow evolution. In Fig. 9, the flow structures characterized by regions of $u > 0$ and $u < 0$ extend significantly in the x direction at $t/t_r = 320$, indicating the development of ELSS. These ELSS differ from the typical large-scale structures (LSS) of turbulent shear flows, which exhibit less anisotropy than ELSS.[25,35] The ELSS and LSS are also distinguishable by their streamwise length scales, as revealed through spectral analysis below. At $t/t_r = 320$, the regions with $u > 0$ and $u < 0$ reach lengths of approximately $100h_0$. However, because the domain size $L_x = 448h_0$ is larger than these structures, multiple ELSS with alternating signs of u are observed along the x direction. As a result, the periodic boundaries are unlikely to influence the ELSS in Re12Lx448. In contrast, for $L_x = 112h_0$ (Fig. 8), the development of ELSS is affected by the domain size. Up to $t/t_r = 200$, the velocity distributions for $L_x = 112h_0$ and $448h_0$ are similar. However, at $t/t_r = 320$, the flow structures in Re12Lx112 are noticeably shorter in the x direction, indicating that ELSS growth is suppressed. This suppression is expected, as the ELSS observed in Re12Lx448 exceed $100h_0$, which is more than half the domain length in Re12Lx112. These comparisons show that ELSS with streamwise lengths on the order of $\mathcal{O}(10^2 h_0)$ do not develop when the domain size is insufficiently large. This allows for a direct examination of how ELSS influence flow behavior by comparing cases with and without the presence of ELSS.

B. One-point statistics of velocity and density

One-point statistics of velocity and density are compared across different L_x cases. Figure 10(a) shows the vertical profiles of the mean streamwise velocity $\langle u \rangle$ for Re12Lx28 at several time instances. At $t/t_r = 30$, the mean velocity exhibits a sharp gradient across the shear layer. Over time, up to approximately $t/t_r = 220$, the profile gradually becomes more diffused due to turbulent mixing of streamwise momentum. From $t/t_r = 220$ to 320, the profile remains nearly unchanged, indicating a suppression of vertical momentum transport. This evolution of the mean velocity is consistent with previous studies on stably stratified

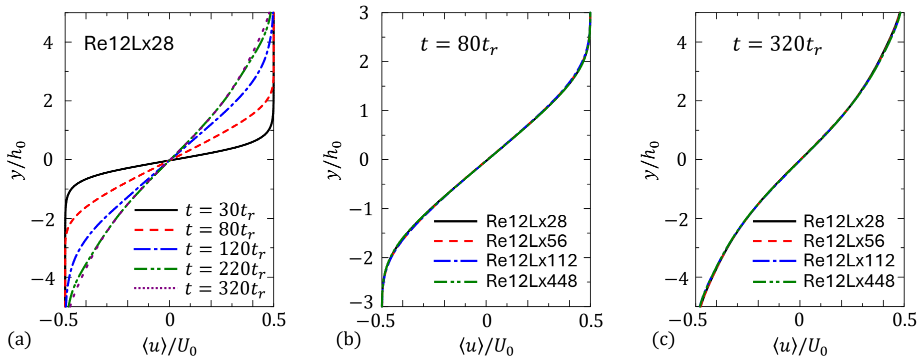

FIG. 10. Vertical profiles of mean streamwise velocity $\langle u \rangle$: (a) temporal evolution in Re12Lx28; (b),(c) L_x dependence at (b) $t/t_r = 80$ and (c) $t/t_r = 320$.

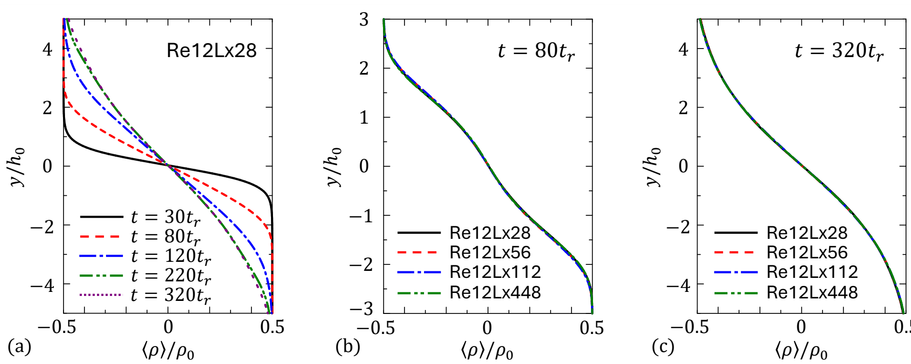

FIG. 11. Vertical profiles of mean density $\langle \rho \rangle$: (a) temporal evolution in Re12Lx28; (b),(c) L_x dependence at (b) $t/t_r = 80$ and (c) $t/t_r = 320$.

shear layers.[25] Figures 10(b) and (c) compare the mean velocity profiles among the different L_x cases with $Re = 1200$ at $t/t_r = 80$ and 320. These comparisons reveal that the mean velocity profiles exhibit no significant variation with changes in the streamwise domain size.

Figure 11(a) presents mean density profiles for the same time instances and case (Re12Lx28) as in Fig. 10(a). The temporal evolution of the mean density profile resembles that of the mean velocity: as the turbulent shear layer develops, vertical transport of density results in a broader distribution. Figures 11(b) and (c) compare the mean density

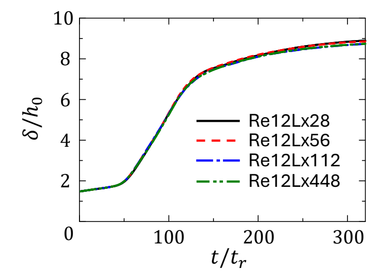

FIG. 12. Temporal variations of the shear layer thickness δ.

profiles among different L_x cases with $Re = 1200$ at $t/t_r = 80$ and 320. As with the mean velocity, the streamwise domain size has minimal influence on the mean density distribution.

The shear layer thickness δ is defined from the mean velocity profile $\langle u \rangle$ as the distance between the locations where $\langle u \rangle/U_0 = -0.45$ and 0.45 in Fig. 10. Figure 12 shows the temporal evolution of δ, normalized by the initial shear layer thickness h_0, for $Re = 1200$. The thickness increases rapidly after $t/t_r = 50$ and continues to grow until around $t/t_r = 150$, after which the growth slows. The initial rapid increase corresponds to the development of large-scale vortices from the KH instability. Subsequently, buoyancy suppresses large-scale vertical motions, thereby limiting further shear layer growth. This trend is consistent with previous findings.[9] Since the mean velocity profile shows negligible dependence on L_x, the shear layer thickness δ is also largely unaffected by the streamwise domain size.

Figure 13 shows the temporal evolution of root mean square (rms) fluctuations of the velocity components (u, v, w) and density ρ at the center of the shear layer for $Re = 1200$. The rms fluctuations are defined as $f_{rms} = \sqrt{\langle f'^2 \rangle}$, where $f' = f - \langle f \rangle$. These rms values increase initially as the turbulent shear layer develops, then decrease due to turbulence decay. Except for u_{rms} in Re12Lx28 after $t/t_r = 190$, the rms values do not show significant variation across the different L_x cases. In Re12Lx28, the decline in u_{rms} slows after $t/t_r = 190$. This behavior corresponds to the point at which the streamwise flow structures grow to the size of the domain in the x direction, as discussed further below. The rms values of v, w, and ρ are less sensitive to L_x than u_{rms}. The streamwise scales of v and w correspond to the transverse scales of turbulence, whereas that of u represents the longitudinal scale. At large scales, the transverse scales are generally much smaller than the longitudinal scale.[35] Therefore, the

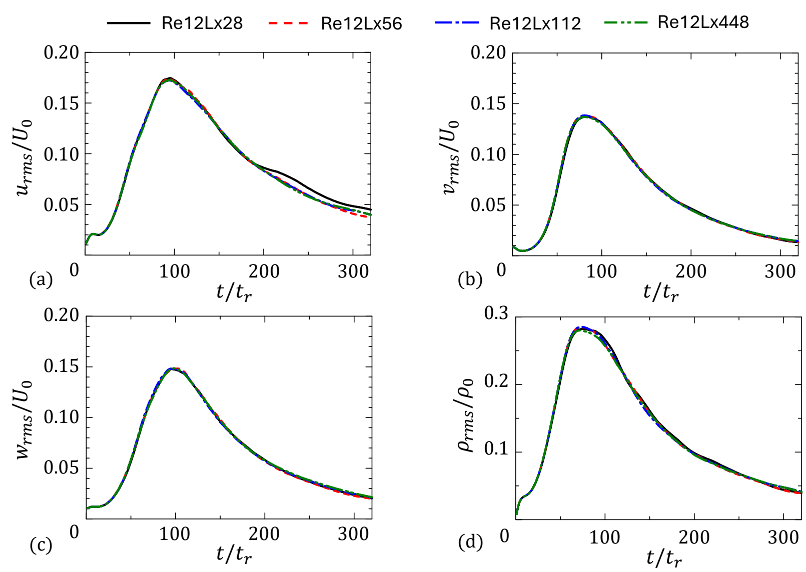

FIG. 13. Temporal variations of rms fluctuations of velocity and density, (a) u_{rms}, (b) v_{rms}, (c) w_{rms}, and (d) ρ_{rms}, at the center of the shear layer, $y = 0$.

larger characteristic scale of u in the streamwise direction likely leads to the more noticeable dependence of u_{rms} on L_x.

Figure 14 presents the vertical profiles of rms streamwise velocity fluctuations at different time instances. The fluctuations are highest within the shear layer centered at $y = 0$ and decrease toward the outer regions. The asymmetry in the statistical profiles between the lower and upper edges of the shear layer arises from statistical uncertainty due to the finite number of samples. Although ensemble averaging over multiple simulations helps reduce such discrepancies, it does not completely eliminate them. At $t/t_r = 80$ in Fig. 14(a), differences among the domain sizes are minimal. However, after $t/t_r = 200$, as shown in Figs. 14(b) and (c), u_{rms} in Re12Lx28 increases relative to the other cases. This increase is confined to the inner region $|y/h_0| < 5$ of the turbulent shear layer. The outer region $|y/h_0| > 5$ is intermittent, meaning that both turbulent and non-turbulent fluid are observed.[81] These two regions are generally separated by the thin interface, whose properties have been investigated in various flows,[82–88] including stratified flows.[57,81,89–97] Previous DNS studies have shown that the

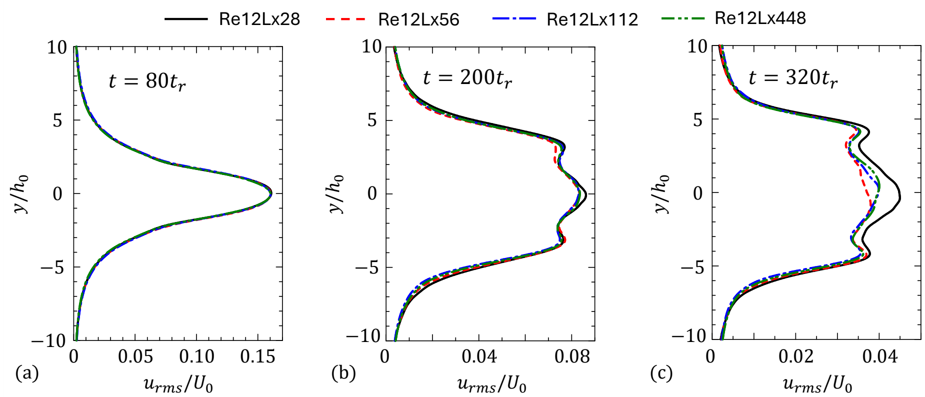

FIG. 14. Vertical profiles of rms fluctuations of u, u_{rms}, at (a) $t/t_r = 80$, (b) $t/t_r = 200$, and (c) $t/t_r = 320$.

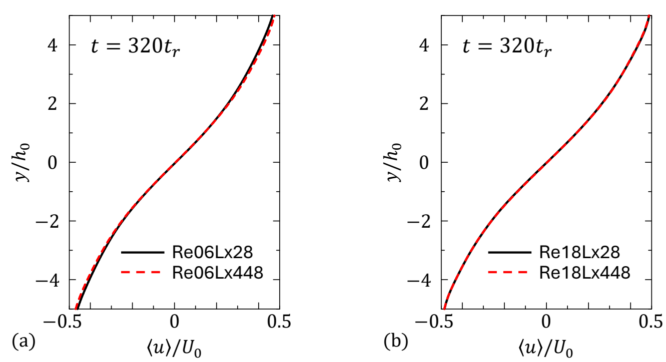

FIG. 15. Vertical profiles of mean streamwise velocity $\langle u \rangle$ at $t/t_r = 320$: (a) $Re = 600$; (b) $Re = 1800$.

characteristc length scale decreases in this intermittent region.[25,35] Therefore, confinement effects in Re12Lx28 have limited impact on u_{rms} in the outer region, where the fluctuations remain largely unaffected by the domain size. Moreover, turbulence characteristics exhibit only a weak dependence on y within the shear layer itself.[25,35] As a result, analyses performed at different vertical positions within the shear layer yield similar outcomes. Hence, the following discussion focuses on the center of the shear layer at $y = 0$.

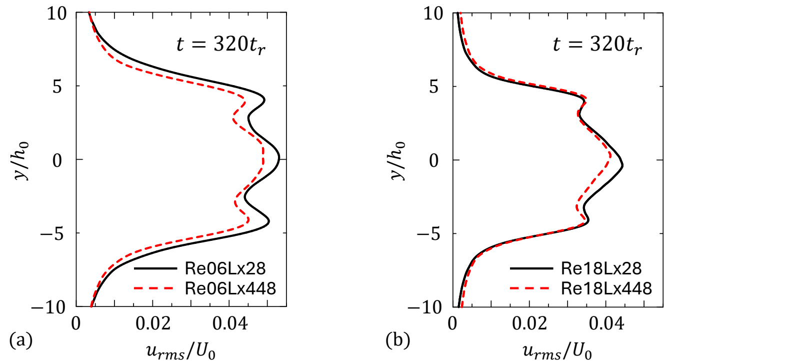

FIG. 16. Vertical profiles of rms fluctuations of u, u_{rms}, at $t/t_r = 320$: (a) $Re = 600$; (b) $Re = 1800$.

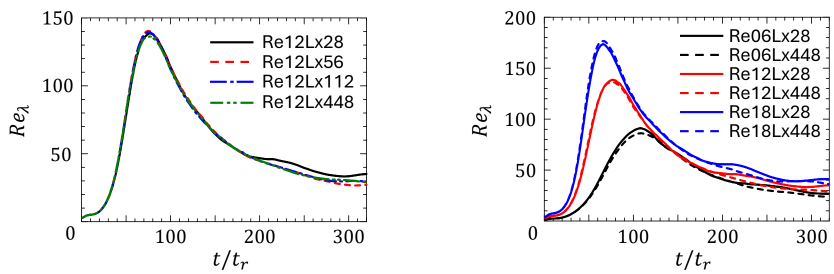

FIG. 17. Temporal variations of the turbulent Reynolds number Re_λ, at the center of the shear layer, $y = 0$: (a) L_x dependence for $Re = 1200$; (b) Re dependence for $L_x/h_0 = 28$ and 448.

Figures 15 and 16 compare the vertical profiles of the mean and rms fluctuations of streamwise velocity at $t/t_r = 320$ for the other Re cases. The mean velocity profiles show minimal dependence on L_x for both Re values. In contrast, the rms velocity fluctuations increase at small L_x. This L_x dependence for $Re = 600$ and 1800 is consistent with that observed for $Re = 1200$ discussed above.

Figure 17 presents the temporal evolution of the turbulent Reynolds number $Re_\lambda = u_{rms}\lambda_x/\nu$ at the shear layer center, where $\lambda_x = u_{rms}/(\partial u/\partial x)_{rms}$ is the Taylor microscale. Re_λ is commonly used to characterize the scale separation between large and small turbulent motions. In Fig. 17(a), results for $Re = 1200$ are compared across different L_x values, while Fig. 17(b) shows results for all Re cases with $L_x/h_0 = 28$ and 448. During the transition phase, Re_λ reaches peak values of approximately 90, 140, and 180 for Re = 600, 1200, and 1800, respectively. Afterward, Re_λ decreases with time due to turbulence decay. At $t/t_r = 320$, the corresponding Re_λ values are 22, 29, and 36 for Re = 600, 1200, and 1800 in the $L_x/h_0 = 448$ cases. As shown in Fig. 17(a), Re_λ exhibits sensitivity to L_x when the streamwise length is as small as $28h_0$, primarily due to the increased u_{rms} for $L_x/h_0 = 28$ (see Fig. 14). A similar L_x dependence is observed for other Re values at later times in Fig. 17(b).

C. Spectra and two-point correlations

The development of ELSS is analyzed using energy spectra. In this study, the Fourier transform is applied in the x direction. The Fourier transform of a variable f in the x direction is denoted by $\hat{u}(k_x, y, z, t)$, and its complex conjugate by $\hat{u}^*$, where k_x is the streamwise wavenumber. The one-dimensional energy spectrum of u is calculated as

$$E_u(k_x, y, t) = \mathrm{Re}[\langle \hat{u}\hat{u}^* \rangle], \tag{2}$$

where the average $\langle \cdot \rangle$ is taken over the z direction, and $\mathrm{Re}(f)$ denotes the real part of the complex variable f. The spectra are presented as functions of wavelength $\lambda_x = 2\pi/k_x$. To assess the contribution of different scales to the total energy, the spectra are premultiplied by the wavenumber k_x, enabling clearer visualization in semi-logarithmic plots.[25,38,98]

Figure 18 presents the streamwise-wavenumber spectrum $k_x E_u(k_x)$ at the center of the shear layer for Re = 1200, plotted against the wavelength λ_x normalized by the initial shear layer thickness h_0. The range of λ_x differs for each case, as the maximum resolvable wavelength is determined by the domain size L_x. At $t/t_r = 120$ in Fig. 18(a), the spectra exhibit similar distributions across all cases, with a dominant peak at $\lambda_x/h_0 \approx$ 10–20. This wavelength is approximately twice the shear layer thickness δ, and the peak corresponds to LSS, the typical large-scale structures in turbulent shear layers. However, for Re12Lx28, the peak is reduced compared to the other cases. Since the domain size in Re12Lx28 is only slightly larger than the LSS scale, the confinement effect partially suppresses the development of these structures, resulting in a smaller spectral peak. This also leads to the different behaviour of u_{rms} in Re12Lx28 shown in Fig. 13(a). In contrast, the domain sizes in Re12Lx56, Re12Lx112, and Re12Lx448 are sufficiently larger than the LSS scale, and thus

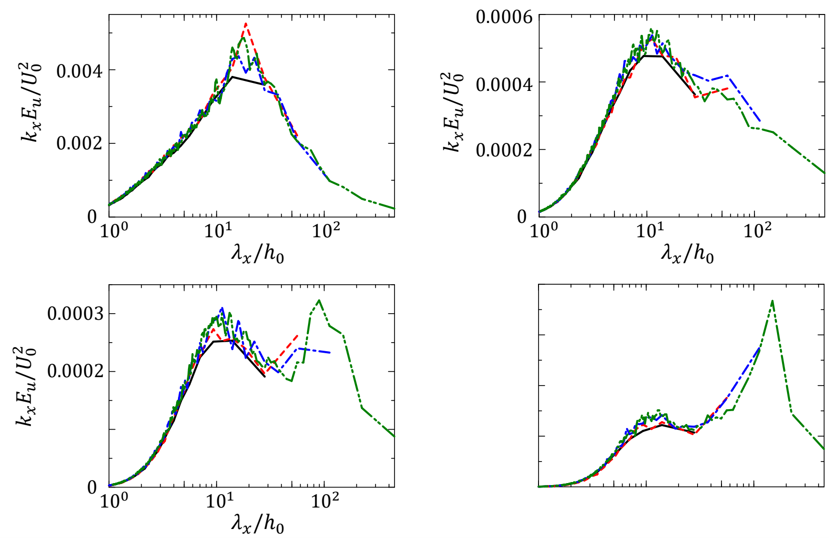

FIG. 18. Premultiplied streamwise-wavenumber spectra of streamwise velocity $k_x E_u(k_x)$ at the center of the shear layer ($Re = 1200$) at (a) $t/t_r = 120$, (b) $t/t_r = 240$, (c) $t/t_r = 280$, and (d) $t/t_r = 320$. The spectra are plotted against wavelength $\lambda_x = 2\pi/k_x$.

the LSS are unaffected by confinement. As the flow evolves, the spectral shape changes significantly. By $t/t_r = 240$ in Fig. 18(b), the energy at large wavelengths ($\lambda_x/h_0 \gtrsim 30$) increases, leading to the emergence of a secondary spectral peak at $\lambda_x/h_0 \approx 50$–100 in Figs. 18(c) and (d) at $t/t_r = 280$ and 320. This secondary peak is associated with the formation of ELSS, as previously discussed in connection with Fig. 9. In Re12Lx448, the ELSS peak is clearly captured, while in Re12Lx56 and Re12Lx112, the domain size is insufficient to fully resolve this spectral feature, although energy growth at the highest available wavelengths is similar among Re12Lx56, Re12Lx112, and Re12Lx448 in Fig. 18(b). Furthermore, the peak wavelength associated with ELSS in Re12Lx448 increases over time, reflecting the continued growth of these structures, which does not occur in Re12Lx56 and Re12Lx112. These comparisons indicate that the energy distribution across streamwise scales cannot be accurately evaluated in Re12Lx28, Re12Lx56, and Re12Lx112 due to the large-scale cutoff imposed by the limited domain size, which inhibits the full development of ELSS.

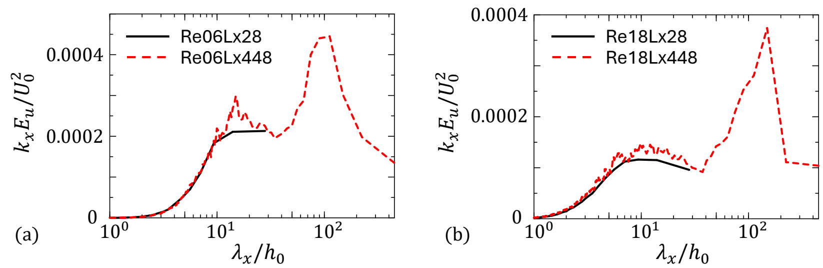

FIG. 19. Premultiplied streamwise-wavenumber spectra of streamwise velocity $k_x E_u(k_x)$ at the center of the shear layer at $t/t_r = 320$: (a) $Re = 600$; (b) $Re = 1800$.

Figures 19(a) and (b) present the energy spectra at $t/t_r = 320$ for $Re = 600$ and 1800, respectively. Each figure compares the spectra for $L_x/h_0 = 28$ and 448. A bimodal spectral shape is observed for $L_x/h_0 = 448$, indicating the presence of ELSS for both Reynolds numbers. The spectral energy at small scales ($\lambda_x/h_0 \lesssim 5$) is higher for the larger Re due to increased scale separation between large and small turbulent motions. The peak associated with the ELSS, located around $\lambda_x/h_0 \approx 10^2$, differs slightly between $Re = 600$ and 1800. Such variation in the ELSS peak wavelength with Reynolds number has also been reported in previous LES and DNS studies of stably stratified shear layers.[25,35] These studies have shown that the spectral shape remains qualitatively similar even at $Re = 40000$. Additionally, the L_x dependence observed in Fig. 19 is consistent with the trends discussed earlier for $Re = 1200$.

The wavelengths of the first and second peaks of the premultiplied energy spectra $k_x E_u(k_x)$ at large t in Fig. 18 correspond to LSS and ELSS, respectively. The shorter peak wavelength, Λ_{LSS}, located near $10h_0$, is associated with LSS. The longer peak wavelength, detectable only in cases with large L_x, is attributed to ELSS and denoted by Λ_{ELSS}. Figure 20 shows the temporal evolution of Λ_{LSS} and Λ_{ELSS}, normalized by the shear layer thickness δ, for $Re = 1200$. For Λ_{ELSS}, data are shown only at time instances where both spectral peaks are clearly identifiable. The transition to fully developed turbulence from the KH instability is largely complete by $t/t_r \approx 100$. After this point, the length scale of LSS, Λ_{LSS}, increases until approximately $t/t_r = 160$. Beyond this point, as the ELSS begin to emerge, the scale separation between the LSS and ELSS increases: the ELSS continue to

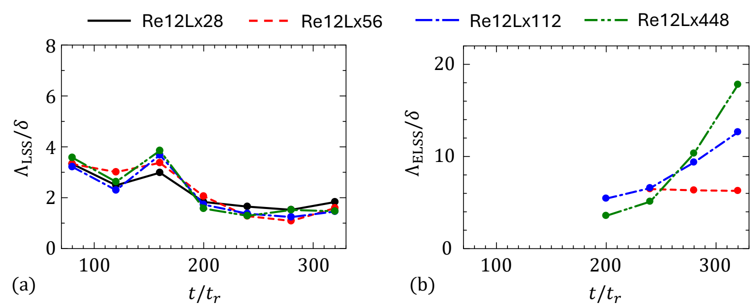

FIG. 20. Temporal variations of the peak wavelengths in energy spectra associated with (a) LSS (Λ_{LSS}) and (b) ELSS (Λ_{ELSS}) for $Re = 1200$.

grow, while the scale of LSS decreases.[25] This interplay gives rise to the observed bump in Λ_{LSS} around $t/t_r = 160$. In Re12Lx112 and Re12Lx448, the ELSS-related peak appears after $t/t_r = 200$, and in Re12Lx56, it appears after $t/t_r = 240$. In Re12Lx28, the ELSS peak is not observed, as L_x is much smaller than the typical ELSS length. As shown in Fig. 20(a), Λ_{LSS} gradually decreases after $t/t_r = 160$ and reaches a nearly constant ratio of $\Lambda_{\text{LSS}}/\delta \approx 1.5$, consistent across all cases. This decrease coincides with the onset of ELSS formation and suggests a growing scale separation between LSS and ELSS as the latter elongates over time. In contrast, the long peak wavelength Λ_{ELSS}, shown in Fig. 20(b), is strongly dependent on L_x. In Re12Lx448, Λ_{ELSS} increases rapidly with time, reflecting the continuous growth of ELSS. This growth is increasingly suppressed as L_x decreases, indicating the influence of confinement effects on ELSS development. The weak dependence of Λ_{LSS} on L_x suggests that LSS, which scale with the shear layer thickness, evolve independently of ELSS. This implies limited interaction between structures at the LSS and ELSS scales.

The time scale of the ELSS based on the streamwise length is estimated as $T_{\text{ELSS}} = \Lambda_{\text{ELSS}}/u_{rms}$. At $t/t_r = 320$, this time scale is found to be $T_{\text{ELSS}}/t_r = 3.9 \times 10^3$ in Re12Lx448. The ELSS exhibits a much larger time scale than the reference time scale of the stably stratified shear layer, t_r. Owing to its large time scale, the ELSS is continuously distorted by the mean shear, whose characteristic time scale, $T_S = \delta/U_0 \approx 9$, is much shorter than T_{ELSS}. This rapid distortion leads to significant increase in the ELSS length scale observed in the present study.

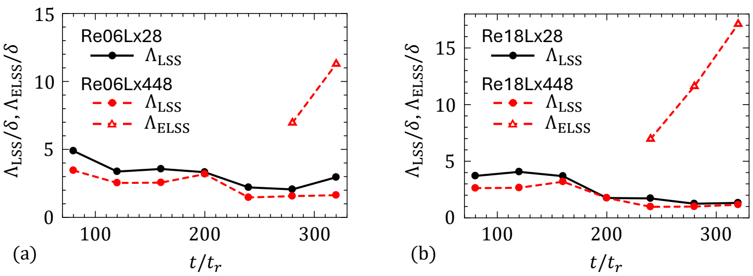

FIG. 21. Temporal variations of $\Lambda_{\rm LSS}$ and $\Lambda_{\rm ELSS}$ for (a) $Re = 600$ and (b) $Re = 1800$.

Figures 21(a) and (b) present the temporal evolution of $\Lambda_{\rm LSS}$ and $\Lambda_{\rm ELSS}$ for $Re = 600$ and 1800, respectively. Each figure compares the results for $L_x/h_0 = 28$ and 448. The spectral peak associated with the ELSS emerges at $t/t_r = 280$ and 240 for $Re = 600$ and 1800, respectively. Accordingly, the plots of $\Lambda_{\rm ELSS}$ for $L_x/h_0 = 448$ are shown after these times. As observed for the $Re = 1200$ case, $\Lambda_{\rm ELSS}$ increases with time, whereas $\Lambda_{\rm LSS}$ exhibits a slight decrease. The scale separation between the LSS and ELSS increases over time due to the growth of the ELSS. At $t/t_r = 320$, the length scale ratios $\Lambda_{\rm ELSS}/\Lambda_{\rm LSS}$ are approximately 7, 12, and 15 for $Re = 600$, 1200, and 1800, respectively. The larger ratio at higher Re is attributed to the faster transition to turbulence, as shown in Fig. 17. At a given time, the turbulence in higher-Re cases has evolved for a longer period after the transition, thereby experiencing mean shear effects over a longer duration, which leads to greater anisotropy and larger values of $\Lambda_{\rm ELSS}/\Lambda_{\rm LSS}$.

In physical space, flow structures are often analyzed using two-point velocity correlation functions. This study considers the longitudinal and transverse auto-correlation functions of the streamwise velocity u, denoted as R_{ux} and R_{uz}, respectively. These functions are defined as

$$R_{ux}(r_x, y, t) = \frac{\langle u'(x, y, z, t)\, u'(x + r_x, y, z, t)\rangle}{u_{rms}^2(y, t)},$$
$$R_{uz}(r_z, y, t) = \frac{\langle u'(x, y, z, t)\, u'(x, y, z + r_z, t)\rangle}{u_{rms}^2(y, t)}, \tag{3}$$

where r_x and r_z are separation distances in the x and z directions, respectively.

Figure 22 shows the longitudinal auto-correlation function R_{ux} for various L_x cases with $Re = 1200$. The range of r_x is limited to $0 \le r_x \le L_x/2$, since separations greater than $L_x/2$ are effectively reduced to $L_x - r_x$ by the periodic boundary condition.[80] The correla-

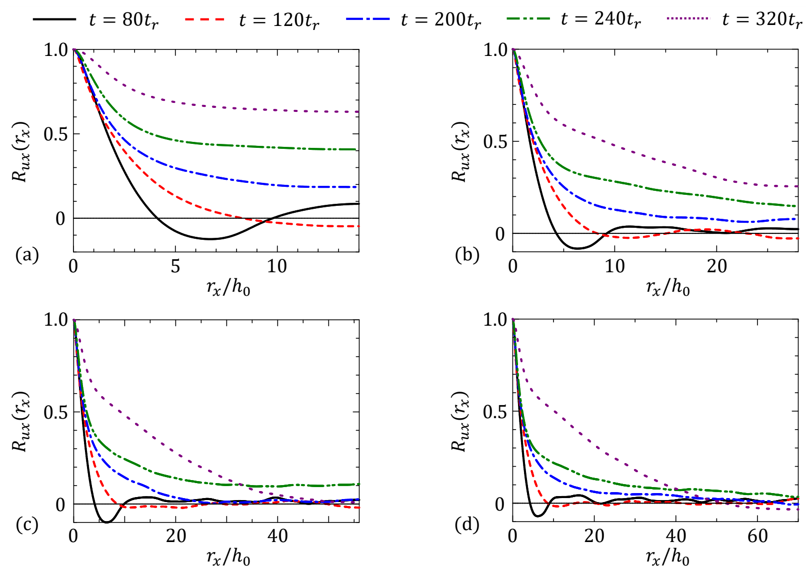

FIG. 22. Longitudinal auto-correlation functions of streamwise velocity, $R_{ux}(r_x, y, t)$, at $y = 0$ in (a) Re12Lx28, (b) Re12Lx56, (c) Re12Lx112, and (d) Re12Lx448.

tion function with large r_x increases with time, indicating the growth of the characteristic streamwise length scale. In Re12Lx28 and Re12Lx56, shown in Figs. 22(a) and (b), R_{ux} does not decay to zero within the available r_x range, indicating that the domain size is insufficient to accommodate the full extent of large streamwise structures such as ELSS. In contrast, Re12Lx448, shown in Fig. 22(d), exhibits well-resolved correlation profiles even at later times, confirming that the domain is large enough to contain the elongated structures.

Figure 23 compares the transverse auto-correlation functions R_{uz} at the same time instances as in Fig. 22. Across all cases, the domain size has no significant qualitative effect on the transverse correlations. Alternating positive and negative u values due to the ELSS in the spanwise direction lead to oscillations of R_{uz} between positive and negative values at larger r_z. A similar correlation profile was also reported for a non-stratified turbulent shear layer.[99] Starting from $r_z = 0$, R_{uz} decreases from 1 to 0 as r_z increases. At $t/t_r = 320$, the first zero-crossing occurs at $r_z/h_0 = 9.0$ for Re12Lx28 and 8.0 for Re12Lx448. The longer spanwise length scale in Re12Lx28 indicates that, in the absence of well-developed ELSS,

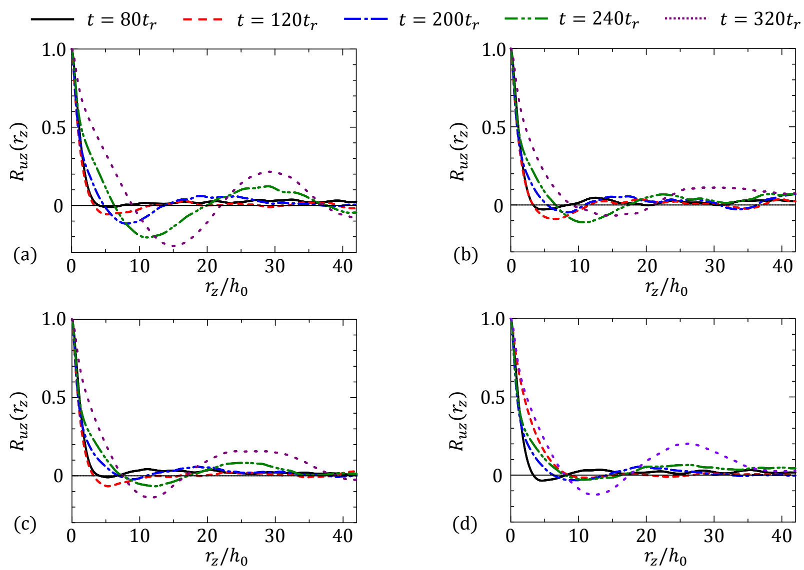

FIG. 23. Transverse auto-correlation functions of streamwise velocity, $R_{uz}(r_z, y, t)$, at $y = 0$ in (a) Re12Lx28, (b) Re12Lx56, (c) Re12Lx112, and (d) Re12Lx448.

the spacing between flow structures increases. Beyond the first zero-crossing, R_{uz} reaches a minimum value, and the location of this minimum corresponds to the typical spanwise separation between adjacent ELSS with opposite signs of u. The minima occur at $r_z/h_0 = 15.0$ in Re12Lx28 and 12.2 in Re12Lx448. This suggests that the center-to-center spacing between alternating positive and negative u structures becomes larger when the ELSS do not fully develop, consistent with the visual patterns observed in Figs. 7 and 9.

To further examine the spatial distribution of ELSS, the two-dimensional auto-correlation function is evaluated as

$$R_{uxz}(r_x, r_z, y, t) = \frac{\langle u'(x, y, z, t)\, u'(x + r_x, y, z + r_z, t)\rangle}{u^2_{rms}(y, t)}. \tag{4}$$

Figure 24 compares this correlation at $y = 0$ for different L_x cases with $Re = 1200$. For Re12Lx112 and Re12Lx448, the positive correlation near $(r_x, r_z) = (0, 0)$ exhibits an "X" pattern, reflecting the meandering behavior of the ELSS. These structures are slightly inclined from the streamwise (x) direction, as also seen in Fig. 9. This correlation pattern is similar to that observed for superstructures in turbulent boundary layers.[41] The ridge of

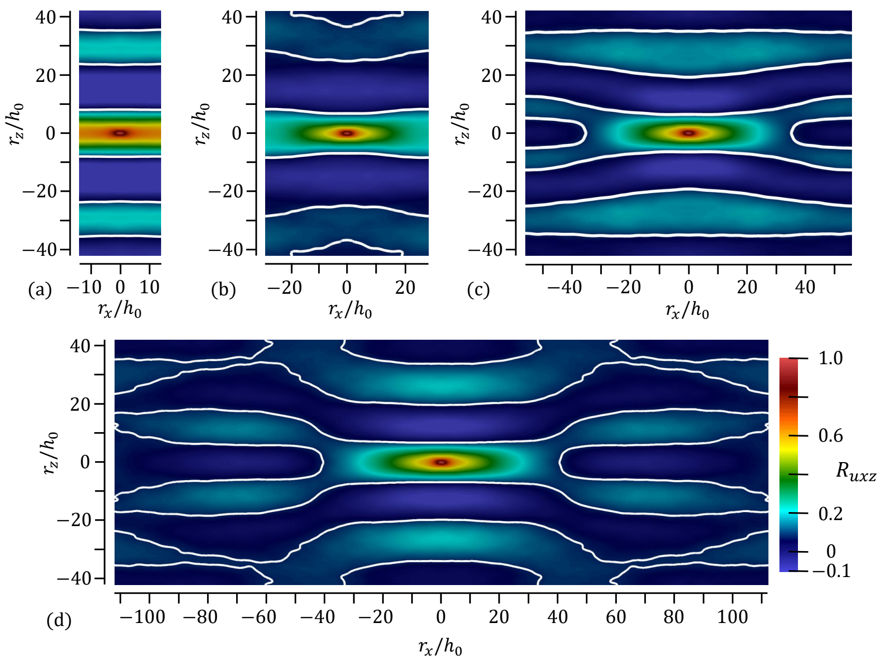

FIG. 24. Two-dimensional auto-correlation functions of streamwise velocity, $R_{uxz}(r_x, r_z, y, t)$, at $y = 0$ and $t/t_r = 320$ in (a) Re12Lx28, (b) Re12Lx56, (c) Re12Lx112, and (d) Re12Lx448.

R_{uxz} represents the inclination of the ELSS. At $r_x = 50h_0$, $R_{uxz}(r_z)$ peaks at $r_z = 9.3h_0$ for Re12Lx448, indicating that the ELSS is inclined at approximately 10 degrees from the x-axis. This inclination angle is comparable to that reported for superstructures in turbulent boundary layers.[41] In contrast, the “X” pattern does not appear in Re12Lx28 and Re12Lx56. In these smaller domains, the meandering feature cannot be captured due to confinement, and the ELSS are artificially connected across the periodic boundaries.

The longitudinal and transverse integral scales of the streamwise velocity are defined as the integrals of the auto-correlation functions $R_{ux}(r_x)$ and $R_{uz}(r_z)$, respectively:

$$L_{Ix} = \int_0^{r_{x0}} R_{ux}(r_x)\, dr_x, \quad L_{Iz} = \int_0^{r_{z0}} R_{uz}(r_z)\, dr_z. \tag{5}$$

Because the correlation profiles vary depending on the flow configuration, different methods have been used in previous studies to determine the integration limits r_{x0} and r_{z0}.[100] One

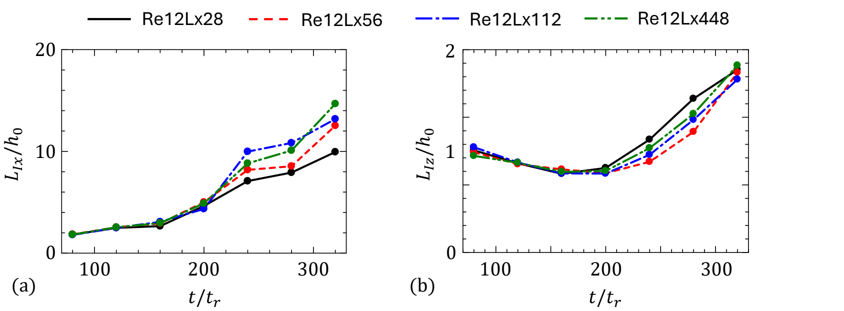

FIG. 25. Temporal variations of (a) longitudinal and (b) transverse integral scales of streamwise velocity for $Re = 1200$.

common approach is to use the smallest separation distance at which the correlation function becomes zero.[101,102] However, this method can be sensitive to oscillations that appear in the correlation at large separations. To avoid this issue, alternative methods integrate up to a fixed threshold value of the correlation function, beyond which the contribution is considered insignificant.[103,104] In this study, we adopt this second approach and define r_{x0} and r_{z0} as the separation distances at which $R_{ux} = 0.05$ and $R_{uz} = 0.05$, respectively. If R_{ux} does not reach zero due to the limited domain size L_x, the integral is computed up to $r_{x0} = L_x/2$. While different choices for the integration range can slightly affect the computed integral scales, the overall conclusions discussed below remain unaffected.

Figure 25 shows the temporal evolution of the integral length scales for $Re = 1200$ after $t/t_r = 80$, a period during which three-dimensional turbulence has developed from the initial KH instability. The streamwise integral scale L_{Ix}, shown in Fig. 25(a), does not vary significantly across different L_x cases until $t/t_r = 200$. After approximately $t/t_r = 200$, as the ELSS begin to grow, L_{Ix} starts to diverge among the cases. Specifically, in simulations with smaller L_x, the growth of L_{Ix} is suppressed relative to Re12Lx448, due to the inhibition of ELSS development by confinement effects. The spanwise integral scale L_{Iz}, presented in Fig. 25(b), exhibits a different trend. A slight decrease in L_{Iz} is observed up to $t/t_r = 200$, followed by a gradual increase. This behavior is consistent across all L_x cases. However, differences between the cases become more pronounced after $t/t_r = 200$, when the ELSS begin to grow. These results indicate that the spanwise organization of very large-scale

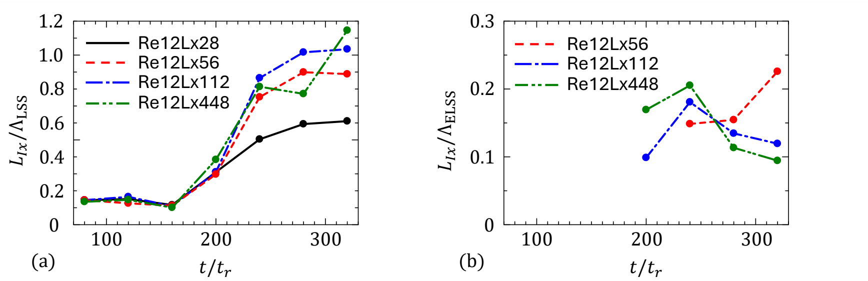

FIG. 26. Temporal variations of the longitudinal integral scale of streamwise velocity normalized by (a) Λ_{LSS} and (b) Λ_{ELSS} for $Re = 1200$.

velocity fluctuations is also affected when ELSS development is constrained by the limited domain size.

Figure 26 compares the longitudinal integral scale of the streamwise velocity, L_{Ix}, with the characteristic wavelengths Λ_{LSS} and Λ_{ELSS} by plotting the normalized quantities $L_{Ix}/\Lambda_{\mathrm{LSS}}$ and $L_{Ix}/\Lambda_{\mathrm{ELSS}}$ as functions of time. If the integral scale correlates with either of these wavelengths, the corresponding normalized value remains approximately constant over time. In the early stage, up to $t/t_r = 160$, $L_{Ix}/\Lambda_{\mathrm{LSS}}$ remains nearly constant at approximately 0.18, indicating that the spatial correlation length scales with the size of the LSS. As the ELSS begin to develop after this point, $L_{Ix}/\Lambda_{\mathrm{LSS}}$ increases rapidly. This increase reflects the growing influence of ELSS on the streamwise velocity correlation at large separation distances. Since the growth of ELSS is influenced by the domain size, $L_{Ix}/\Lambda_{\mathrm{LSS}}$ varies across different L_x cases. However, in cases where the ELSS are captured in Re12Lx448, $L_{Ix}/\Lambda_{\mathrm{ELSS}}$ remains approximately between 0.1 and 0.2, while $L_{Ix}/\Lambda_{\mathrm{LSS}}$ increases from about 0.2 to 1.2. This result indicates that once the ELSS are sufficiently developed, the streamwise integral scale becomes correlated with the ELSS length scale rather than that of the LSS.

D. Parameters characterizing turbulence and mixing

The above results confirm that a small streamwise domain inhibits the development of ELSS, effectively removing these structures and altering the large-scale flow characteristics. To further understand the role of ELSS, the present study investigates the energy dissipation coefficient and mixing parameters, aiming to clarify how the presence or absence of ELSS influences the turbulence properties and mixing processes.

The energy dissipation coefficient is defined by normalizing the turbulent kinetic energy dissipation rate $\varepsilon = \langle \nu(\partial u_i'/\partial x_j)^2 \rangle$ with characteristic velocity and length scales $\mathcal{U}$ and $\mathcal{L}$ of large scales, as

$$C_\varepsilon = \frac{\varepsilon}{\mathcal{U}^3/\mathcal{L}}. \tag{6}$$

In fully developed turbulence under stable stratification, C_ε tends to remain approximately constant in each flow. In homogeneous turbulence, the physical mechanisms underlying this constancy vary with the Reynolds number. At high Reynolds numbers, it is attributed to a balance between energy cascade and dissipation.[105] At low Reynolds numbers, the dominant contribution of vertical gradients of horizontal velocity to dissipation can also result in a constant dissipation coefficient.[106] In contrast, stably stratified turbulent shear layers differ from homogeneous turbulence in that an active energy cascade can occur even at low Reynolds numbers.[25] The present study investigates how the development of ELSS influences the behavior of the dissipation coefficient. Following previous work of turbulent shear flows,[107] the dissipation coefficient is defined using the streamwise velocity as

$$C_\varepsilon = \frac{\varepsilon}{u_{rms}^3/L_{Ix}}. \tag{7}$$

However, unlike in homogeneous turbulence, the stably stratified shear layer contains two distinct characteristic length scales, those of the LSS and ELSS, which differ from the integral scale L_{Ix}. To assess the influence of these structures, the energy dissipation coefficient is also computed using the LSS and ELSS length scales:

$$C_\varepsilon^{(\mathrm{LSS})} = \frac{\varepsilon}{u_{rms}^3/\Lambda_{\mathrm{LSS}}}, \quad C_\varepsilon^{(\mathrm{ELSS})} = \frac{\varepsilon}{u_{rms}^3/\Lambda_{\mathrm{ELSS}}}. \tag{8}$$

These definitions allow comparison of how each scale contributes to the overall dissipation behavior in the presence or absence of ELSS.

Figure 27(a) shows the temporal evolution of the dissipation coefficient based on the integral length scale, C_ε, for different L_x cases with $Re = 1200$. In all cases, C_ε increases with time until approximately $t/t_r = 280$, corresponding to the rapid growth of the integral length scale, as shown in Fig. 25. For smaller L_x, the values of C_ε remain lower due to the inhibited growth of the integral scale caused by the confinement effect. Figure 27(b) compares the dissipation coefficients defined using the characteristic length scales of ELSS

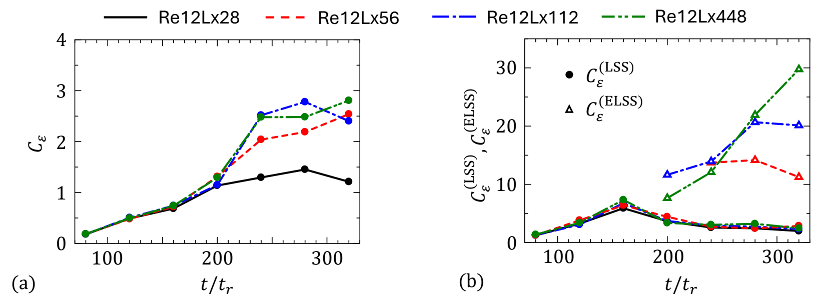

FIG. 27. Temporal variations of the dissipation coefficients defined with (a) the integral length scale L_{Ix}, C_ε, and (b) the length scales of LSS and ELSS, denoted respectively by $C_\varepsilon^{(\mathrm{LSS})}$ and $C_\varepsilon^{(\mathrm{ELSS})}$. The results are compared for different L_x cases with $Re = 1200$.

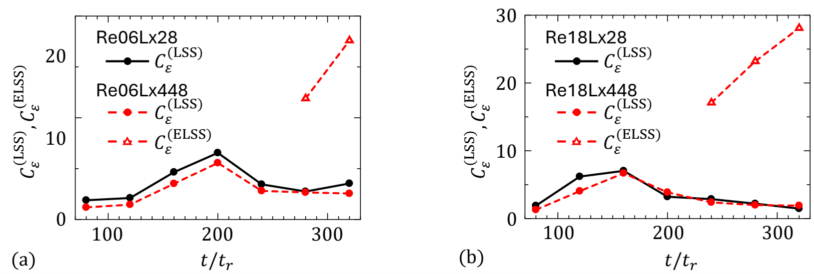

FIG. 28. Temporal variations of $C_\varepsilon^{(\mathrm{LSS})}$ and $C_\varepsilon^{(\mathrm{ELSS})}$ for (a) $Re = 600$ and (b) $Re = 1800$.

and LSS, denoted as $C_\varepsilon^{(\mathrm{ELSS})}$ and $C_\varepsilon^{(\mathrm{LSS})}$, respectively. The values of $C_\varepsilon^{(\mathrm{ELSS})}$ are shown only for time instances where the secondary spectral peak associated with ELSS is identified. When L_x is sufficiently large, $C_\varepsilon^{(\mathrm{ELSS})}$ exhibits an increasing trend over time, consistent with the late-time behavior of C_ε based on the integral scale. In contrast, $C_\varepsilon^{(\mathrm{LSS})}$ remains nearly constant at about 2 after the ELSS have formed.

Figures 28 present the temporal evolution of $C_\varepsilon^{(\mathrm{LSS})}$ and $C_\varepsilon^{(\mathrm{ELSS})}$ for $Re = 600$ and 1800. The results are consistent with those observed for $Re = 1200$: $C_\varepsilon^{(\mathrm{LSS})}$ shows weak time dependence for both $L_x/h_0 = 28$ and 448, even when the ELSS does not develop in the smaller domain. As also seen for $Re = 1200$, $C_\varepsilon^{(\mathrm{ELSS})}$ increases rapidly with time for $Re = 600$ and 1800.

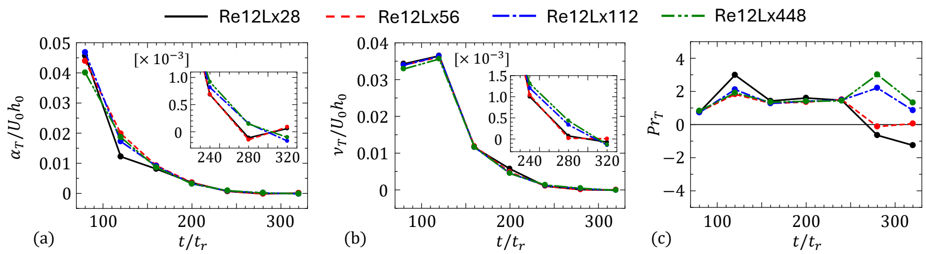

FIG. 29. Temporal variations of (a) eddy diffusivity α_T, (b) eddy viscosity ν_T, and (c) turbulent Prandtl number Pr_T for $Re = 1200$.

The behavior of the dissipation coefficients defined using the three different scales has important implications for the energetics of the stably stratified shear layer. When L_x is small, the development of ELSS is artificially constrained: the ELSS either do not form or their meandering characteristics are not observed. Despite these modifications to the ELSS, the dissipation coefficient based on the LSS scale, $C_\varepsilon^{(\mathrm{LSS})}$, remains nearly constant after the ELSS begin to develop. This result suggests that the energy dissipation rate primarily scales with the LSS, indicating that the LSS are the dominant structures responsible for interscale energy transfer toward the small scales where dissipation occurs.[25] The ELSS, by contrast, do not play a significant role in this process, as evidenced by the negligible dependence of $C_\varepsilon^{(\mathrm{LSS})}$ on the presence or absence of ELSS.

Another important parameter for modeling turbulent mixing is the turbulent Prandtl number, defined as $Pr_T = \nu_T/\alpha_T$, where ν_T and α_T represent the eddy viscosity and eddy diffusivity, respectively. In a stably stratified mixing layer, these quantities are computed as

$$\nu_T = -\frac{\langle u'v'\rangle}{\partial\langle u\rangle/\partial y}, \quad \alpha_T = -\frac{\langle \rho'v'\rangle}{\partial\langle \rho\rangle/\partial y}. \tag{9}$$

These parameters are closely related to the flux Richardson number and mixing efficiency, and play a critical role in modeling and parameterizing turbulent mixing in stably stratified turbulence.[108,109]

Figure 29 shows the temporal evolution of ν_T, α_T, and Pr_T for $Re = 1200$. Temporal variations of the turbulent fluxes $\langle u'v'\rangle$ and $\langle \rho'v'\rangle$, as well as their scale dependence based on cospectral analysis, have been examined in detail in previous studies of the same flow.[25] Both ν_T and α_T generally decrease over time due to the decay of turbulence. At $t/t_r = 80$, when turbulence has fully developed from the initial KH instability, Pr_T is approximately 0.7. Both experiments and numerical simulations of stratified shear flows have reported similar values of Pr_T, supporting the present results.[30,110,111] In Re12Lx112 and Re12Lx448, Pr_T remains positive even after the development of ELSS. However, after $t/t_r > 240$, corresponding to the ELSS formation, deviations are observed in Re12Lx28 and Re12Lx56, where Pr_T no longer matches the trend in larger L_x cases. At $t/t_r = 320$, both ν_T and α_T become negative in Re12Lx112 and Re12Lx448. Classical turbulence models for shear flows typically assume that turbulent momentum and density are transported down the respective mean gradients, implying $\nu_T > 0$ and $\alpha_T > 0$. Negative values of ν_T and α_T indicate counter-gradient diffusion, where momentum and density are transported in the direction opposite to their mean gradients. Previous studies have shown that counter-gradient transport in stably stratified shear layers occurs predominantly at intermediate scales between the LSS and ELSS.[35] The momentum and density fluxes at these intermediate scales drive the negative values of ν_T and α_T, and are strongly influenced by the presence of ELSS, as evidenced by the contrasting behaviors in small and large L_x cases. Although the magnitudes of turbulent momentum and density fluxes decrease over time due to turbulence decay, their relative contributions to the turbulent kinetic energy and density variance remain important. These contributions possibly continue to influence the long-term evolution of the flow.

The budget of turbulent kinetic energy in wavenumber space has shown that inverse energy transfer toward the ELSS scale occurs for the spanwise velocity component.[25] This behavior reflects similarities between stably stratified shear layers and the near-wall regions of wall-bounded turbulent flows, particularly the buffer and logarithmic layers. In these regions, inverse energy transfer in the spanwise velocity component is also observed,[112] and large-scale elongated structures resembling the ELSS are known to exist.[41] Furthermore, the stably stratified shear layer exhibits a k_x^{-1} spectral scaling between the LSS and ELSS scales, mirroring the well-established k_x^{-1} law in wall-bounded turbulent flows.[113] These similarities likely arise from mean shear effects under suppression of vertical turbulent motions, either by walls or buoyancy. This interpretation is supported by observations in wall-confined shear layers, where vertical motions are constrained by parallel walls.[42] As discussed in detail in Ref. 25, these comparisons suggest that the observed inverse energy transfer is a characteristic feature of three-dimensional, shear-driven turbulence.

IV. CONCLUSION

The present study has conducted DNS of a temporally evolving, stably stratified shear layer with various streamwise domain sizes L_x. The fully developed turbulent shear layer features two distinct large-scale length scales: one associated with typical large-scale structures (LSS) with a scale comparable to the shear layer thickness, and the other corresponding to elongated large-scale structures (ELSS) with streamwise lengths significantly greater than those of the LSS. The growth of ELSS is inhibited or modulated when the streamwise domain size is small. By comparing results across different L_x values, the role of ELSS in flow evolution is elucidated. The results show that one-point statistics, such as mean and rms fluctuations of velocity and density, reflect the properties of LSS. Despite the changes in ELSS in the small domains, statistics associated with LSS remain largely unchanged, indicating that LSS evolution is mostly decoupled from the formation of ELSS. The behaviour of dissipation coefficients suggests that energy transfer from large to small scales is primarily driven by LSS, with little contribution from ELSS. However, the counter-gradient diffusion at large scales, associated with length scales between LSS and ELSS,[35] is shown to be related to the development of ELSS and is not captured when ELSS growth is suppressed. In summary, ELSS play a critical role at scales larger than LSS, influencing large-scale streamwise velocity variations. However, turbulence properties at scales smaller than LSS, which dominate energy dissipation, remain largely unaffected by the presence of ELSS.

ACKNOWLEDGMENTS

Numerical simulations were performed by the high-performance computing systems at the Japan Agency for Marine-Earth Science and Technology. This work was supported by JSPS KAKENHI Grant nos JP25K01155 and JP23K22669.

DATA AVAILABILITY

The present DNS databases, including full three-dimensional fields and statistical data, are available from the corresponding author upon reasonable request.

REFERENCES

[1] S. A. Thorpe, "The near-surface ocean mixing layer in stable heating conditions," J. Geophys. Res. **83**, 2875 (1978).

[2] L. Mahrt, "Stratified atmospheric boundary layers," Boundary-Layer Meteorol. **90**, 375 (1999).

[3] J. P. Mellado, "Cloud-top entrainment in stratocumulus clouds," Annu. Rev. Fluid Mech. **49**, 145 (2017).

[4] G. Baumgarten and D. C. Fritts, "Quantifying Kelvin–Helmholtz instability dynamics observed in noctilucent clouds: 1. Methods and observations," J. Geophys. Res. Atmos. **119**, 9324 (2014).

[5] W. D. Smyth and J. N. Moum, "Ocean mixing by Kelvin-Helmholtz instability," Oceanography **25**, 140 (2012).

[6] C. B. Kjellstrand, D. C. Fritts, A. D. Miller, B. P. Williams, N. Kaifler, C. Geach, S. Hanany, B. Kaifler, G. Jones, M. Limon, *et al.*, "Multi-scale Kelvin-Helmholtz instability dynamics observed by PMC turbo on 12 July 2018: 1. Secondary instabilities and billow interactions," J. Geophys. Res. Atmos. **127**, e2021JD036232 (2022).

[7] S. A. Thorpe, "Experiments on instability and turbulence in a stratified shear flow," J. Fluid Mech. **61**, 731 (1973).

[8] E. J. Strang and H. J. S. Fernando, "Entrainment and mixing in stratified shear flows," J. Fluid Mech. **428**, 349 (2001).

[9] W. D. Smyth and J. N. Moum, "Length scales of turbulence in stably stratified mixing layers," Phys. Fluids **12**, 1327 (2000).

[10] H. T. Pham and S. Sarkar, "Large eddy simulations of a stratified shear layer," J. Fluids Eng. **136**, 060913 (2014).

[11] J. Holmboe, "On the behavior of symmetric waves in stratified shear layers," Geofys. Publ. **24**, 67 (1962).

[12] W. D. Smyth and K. B. Winters, "Turbulence and mixing in Holmboe waves," J. Phys. Oceanogr. **33**, 694 (2003).

[13] F. K. Browand and C. D. Winant, "Laboratory observations of shear-layer instability in a stratified fluid," Boundary-Layer Meteorol. **5**, 67 (1973).

[14]A. M. Hogg and G. N. Ivey, "The Kelvin–Helmholtz to Holmboe instability transition in stratified exchange flows," J. Fluid Mech. **477**, 339 (2003).

[15]W. D. Smyth, J. R. Carpenter, and G. A. Lawrence, "Mixing in symmetric Holmboe waves," J. Phys. Oceanogr. **37**, 1566 (2007).

[16]M. Rahmani, B. R. Seymour, and G. A. Lawrence, "The effect of Prandtl number on mixing in low Reynolds number Kelvin-Helmholtz billows," Phys. Fluids **28**, 054107 (2016).

[17]H. Salehipour, C. P. Caulfield, and W. R. Peltier, "Turbulent mixing due to the holmboe wave instability at high Reynolds number," J. Fluid Mech. **803**, 591 (2016).

[18]A. J. K. Yang, E. W. Tedford, J. Olsthoorn, and G. A. Lawrence, "Sensitivity of wave merging and mixing to initial perturbations in Holmboe instabilities," Phys. Fluids **34** (2022).

[19]G. P. Klaassen and W. R. Peltier, "The influence of stratification on secondary instability in free shear layers," J. Fluid Mech. **227**, 71 (1991).

[20]A. Mashayek and W. R. Peltier, "The 'zoo' of secondary instabilities precursory to stratified shear flow transition. Part 1 Shear aligned convection, pairing, and braid instabilities," J. Fluid Mech. **708**, 5 (2012).

[21]A. Mashayek and W. R. Peltier, "The 'zoo'of secondary instabilities precursory to stratified shear flow transition. Part 2 The influence of stratification," J. Fluid Mech. **708**, 45 (2012).

[22]D. C. Fritts, L. Wang, T. S. Lund, and S. A. Thorpe, "Multi-scale dynamics of Kelvin–Helmholtz instabilities. Part 1. Secondary instabilities and the dynamics of tubes and knots," J. Fluid Mech. **941**, A30 (2022).

[23]K. Takamure, Y. Sakai, Y. Ito, K. Iwano, and T. Hayase, "Dissipation scaling in the transition region of turbulent mixing layer," Int. J. Heat Fluid Flow **75**, 77 (2019).

[24]Z. Saeed, E. Weidner, B. A. Johnson, and T. L. Mandel, "Buoyancy-modified entrainment in plumes: Theoretical predictions," Phys Fluids **34** (2022).

[25]T. Watanabe and K. Nagata, "Large-scale characteristics of a stably stratified turbulent shear layer," J. Fluid Mech. **927**, A27 (2021).

[26]W. R. Peltier and C. P. Caulfield, "Mixing efficiency in stratified shear flows," Annu. Rev. Fluid Mech. **35**, 135 (2003).

[27]W. D. Smyth, J. N. Moum, and D. R. Caldwell, "The efficiency of mixing in turbulent patches: Inferences from direct simulations and microstructure observations," J. Phys.

Oceanogr. **31**, 1969 (2001).

[28]M. Rahmani, G. A. Lawrence, and B. R. Seymour, "The effect of Reynolds number on mixing in Kelvin–Helmholtz billows," J. Fluid Mech. **759**, 612 (2014).

[29]H. Salehipour, W. Peltier, and A. Mashayek, "Turbulent diapycnal mixing in stratified shear flows: the influence of Prandtl number on mixing efficiency and transition at high Reynolds number," J. Fluid Mech. **773**, 178 (2015).

[30]H. Salehipour and W. R. Peltier, "Diapycnal diffusivity, turbulent Prandtl number and mixing efficiency in Boussinesq stratified turbulence," J. Fluid Mech. **775**, 464 (2015).

[31]C. B. da Silva, R. J. N. Dos Reis, and J. C. F. Pereira, "The intense vorticity structures near the turbulent/non-turbulent interface in a jet," J. Fluid Mech. **685**, 165 (2011).

[32]W. D. Smyth and J. N. Moum, "Anisotropy of turbulence in stably stratified mixing layers," Phys. Fluids **12**, 1343 (2000).

[33]W. D. Smyth, "Secondary circulations in Holmboe waves," Phys. Fluids **18**, 064104 (2006).

[34]H. T. Pham, S. Sarkar, and K. B. Winters, "Intermittent patches of turbulence in a stratified medium with stable shear," J. Turbul. **13**, N20 (2012).

[35]T. Watanabe, J. J. Riley, K. Nagata, K. Matsuda, and R. Onishi, "Hairpin vortices and highly elongated flow structures in a stably stratified shear layer," J. Fluid Mech. **878**, 37 (2019).

[36]R. R. Taveira and C. B. da Silva, "Kinetic energy budgets near the turbulent/nonturbulent interface in jets," Phys. Fluids **25**, 015114 (2013).

[37]X. Chen, K. Iwano, Y. Sakai, and Y. Ito, "The meandering bend features of large-scale structures and the related coherent structures," Int. J. Heat Fluid Flow **93**, 108915 (2022).

[38]K. Takamure, Y. Ito, Y. Sakai, K. Iwano, and T. Hayase, "Momentum transport process in the quasi self-similar region of free shear mixing layer," Phys. Fluids **30**, 015109 (2018).

[39]W. A. McMullan, J. Mifsud, and M. Angelino, "The growth of the initially turbulent mixing layer: A large eddy simulation study," Phys. Fluids **36**, 115194 (2024).

[40]S. N. Hug, W. A. McMullan, J. Mifsud, and S. J. Garrett, "Resolved scalar mixing in large eddy simulations of the laboratory mixing layer," Phys. Fluids **37**, 045148 (2025).

[41]N. Hutchins and I. Marusic, "Evidence of very long meandering features in the logarithmic region of turbulent boundary layers," J. Fluid Mech. **579**, 1 (2007).

[42]T. Akao, T. Watanabe, and K. Nagata, "Vertical confinement effects on a fully developed turbulent shear layer," Phys. Fluids **34**, 055129 (2022).

[43]J. M. Cimbala, H. M. Nagib, and A. Roshko, "Large structure in the far wakes of two-dimensional bluff bodies," J. Fluid Mech. **190**, 265 (1988).

[44]T. Watanabe and K. Nagata, "The response of small-scale shear layers to perturbations in turbulence," J. Fluid Mech. **963**, A31 (2023).

[45]T. Watanabe, "Efficient enhancement of turbulent entrainment by small-scale shear instability," Journal of Fluid Mechanics **988**, A20 (2024).

[46]T. Watanabe and K. Nagata, "Influences of small-scale shear instability on passive-scalar mixing in a shear-free turbulent front," J. Fluid Mech. **1008**, A20 (2025).

[47]J. Jiménez and P. Moin, "The minimal flow unit in near-wall turbulence," J. Fluid Mech. **225**, 213 (1991).

[48]T. Watanabe, X. Zhang, and K. Nagata, "Direct numerical simulation of incompressible turbulent boundary layers and planar jets at high Reynolds numbers initialized with implicit large eddy simulation," Comput. Fluids **194**, 104314 (2019).

[49]M. J. Lee, J. Kim, and P. Moin, "Structure of turbulence at high shear rate," J. Fluid Mech. **216**, 561 (1990).

[50]M. Hayashi, T. Watanabe, and K. Nagata, "Characteristics of small-scale shear layers in a temporally evolving turbulent planar jet," J. Fluid Mech. **920**, A38 (2021).

[51]X. Zhang, T. Watanabe, and K. Nagata, "Reynolds number dependence of the turbulent/non-turbulent interface in temporally developing turbulent boundary layers," J. Fluid Mech. **964**, A8 (2023).

[52]K. Nakamura, T. Watanabe, and K. Nagata, "Turbulent/turbulent interfacial layers of a shearless turbulence mixing layer in temporally evolving grid turbulence," Phys. Fluids **35** (2023).

[53]Y. Morinishi, T. S. Lund, O. V. Vasilyev, and P. Moin, "Fully conservative higher order finite difference schemes for incompressible flow," J. Comput. Phys. **143**, 90 (1998).

[54]L. Biancofiore, "Crossover between two-and three-dimensional turbulence in spatial mixing layers," J. Fluid Mech. **745**, 164 (2014).

[55]W. A. McMullan, "Spanwise domain effects on the evolution of the plane turbulent mixing layer," Intl. J. Comput. Fluid Dyn. **29**, 333 (2015).

[56]D. C. Fritts, S. A. Wieland, T. S. Lund, S. A. Thorpe, and J. H. Hecht, "Kelvin-Helmholtz billow interactions and instabilities in the mesosphere over the Andes Lidar Observatory: 2. Modeling and interpretation," J. Geophys. Res. Atmos. **126**, e2020JD033412 (2021).

[57]T. Watanabe, J. J. Riley, K. Nagata, R. Onishi, and K. Matsuda, "A localized turbulent mixing layer in a uniformly stratified environment," J. Fluid Mech. **849**, 245 (2018).

[58]J. Jiménez, A. A. Wray, P. G. Saffman, and R. S. Rogallo, "The structure of intense vorticity in isotropic turbulence," J. Fluid Mech. **255**, 65 (1993).

[59]M. Tanahashi, S. Iwase, and T. Miyauchi, "Appearance and alignment with strain rate of coherent fine scale eddies in turbulent mixing layer," J. Turbul. **2**, 1 (2001).

[60]S.-J. Kang, M. Tanahashi, and T. Miyauchi, "Dynamics of fine scale eddy clusters in turbulent channel flows," J. Turbul. **8**, N52 (2007).

[61]R. Jahanbakhshi, N. S. Vaghefi, and C. K. Madnia, "Baroclinic vorticity generation near the turbulent/non-turbulent interface in a compressible shear layer," Phys. Fluids **27**, 105105 (2015).

[62]T. Watanabe, C. B. da Silva, K. Nagata, and Y. Sakai, "Geometrical aspects of turbulent/non-turbulent interfaces with and without mean shear," Phys. Fluids **29**, 085105 (2017).

[63]A. A. Ghira, G. E. Elsinga, and C. B. da Silva, "Characteristics of the intense vorticity structures in isotropic turbulence at high Reynolds numbers," Phys. Rev. Fluids **7**, 104605 (2022).

[64]T. Watanabe, K. Tanaka, and K. Nagata, "Characteristics of shearing motions in incompressible isotropic turbulence," Phys. Rev. Fluids **5**, 072601 (2020).

[65]M. Hayashi, T. Watanabe, and K. Nagata, "The relation between shearing motions and the turbulent/non-turbulent interface in a turbulent planar jet," Phys. Fluids **33** (2021).

[66]D. Fiscaletti, O. R. H. Buxton, and A. Attili, "Internal layers in turbulent free-shear flows," Phys. Rev. Fluids **6**, 034612 (2021).

[67]S. B. Pope, *Turbulent Flows* (Cambridge Univ. Pr., 2000).

[68]K. B. Winters, P. N. Lombard, J. J. Riley, and E. A. D'Asaro, "Available potential energy and mixing in density-stratified fluids," J. Fluid Mech. **289**, 115 (1995).

[69]S. A. Thorpe, "Laboratory observations of secondary structures in Kelvin–Helmhoitz billows and consequences for ocean mixing," Geophys. Astrophys. Fluid Dyn. **34**, 175 (1985).

[70] S. A. Thorpe, "Transitional phenomena and the development of turbulence in stratified fluids: A review," J. Geophys. Res. **92**, 5231 (1987).

[71] D. C. Fritts, L. Wang, T. S. Lund, S. A. Thorpe, C. B. Kjellstrand, B. Kaifler, and N. Kaifler, "Multi-scale Kelvin-Helmholtz instability dynamics observed by PMC turbo on 12 July 2018: 2. DNS modeling of KHI dynamics and PMC responses," J. Geophys. Res. Atmos. **127**, e2021JD035834 (2022).

[72] T. S. Mixa, T. S. Lund, and D. C. Fritts, "Modeling Kelvin Helmholtz instability tube and knot dynamics and their impact on mixing in the lower thermosphere," J. Geophys. Res. **128**, e2023JD039249 (2023).

[73] D. C. Fritts and L. Wang, "Kelvin–Helmholtz instability "tube" and "knot" dynamics. Part II: KHI T&K dynamics in a multiscale gravity wave direct numerical simulation," J. Atmos. Sci. **80**, 2439 (2023).

[74] J. H. Hecht, K. Wan, L. J. Gelinas, D. C. Fritts, R. L. Walterscheid, R. J. Rudy, A. Z. Liu, S. J. Franke, F. A. Vargas, P.-D. Pautet, M. J. Taylor, and G. R. Swenson, "The life cycle of instability features measured from the Andes Lidar Observatory over Cerro Pachon on 24 March 2012," J. Geophys. Res. Atmos. **119**, 8872 (2014).

[75] J. H. Hecht, D. C. Fritts, L. J. Gelinas, R. J. Rudy, R. L. Walterscheid, and A. Liu, "Kelvin–Helmholtz billow interactions and instabilities in the mesosphere over the Andes Lidar Observatory: 1. Observations," J. Geophys. Res. Atmos. **126**, e2020JD033414 (2021).

[76] D. C. Fritts, G. Baumgarten, P.-D. Pautet, J. H. Hecht, B. P. Williams, N. Kaifler, B. Kaifler, C. B. Kjellstrand, L. Wang, M. J. Taylor, and A. D. Miller, "Kelvin–Helmholtz instability " tube " and " knot " dynamics. Part I: Expanding observational evidence of occurrence and environmental influences," J. Atmos. Sci. **80**, 2419 (2023).

[77] D. C. Fritts, L. Wang, T. Lund, and M. A. Geller, "Kelvin–Helmholtz instability "tube" and "knot" dynamics. Part III: Extension of elevated turbulence and energy dissipation into increasingly viscous flows," J. Atmos. Sci. **81**, 1147 (2024).

[78] A. VanDine, H. T. Pham, and S. Sarkar, "Turbulent shear layers in a uniformly stratified background: DNS at high Reynolds number," J. Fluid Mech. **916**, A42 (2021).

[79] X. Wang, J. Guo, J. Wang, and S. Chen, "Turbulent kinetic energy budget in compressible turbulent mixing layers: effects of large-scale structures," J. Fluid Mech. **1003**, A25 (2025).

[80] P. A. Davidson, *Turbulence: An Introduction for Scientists and Engineers* (Oxford Univ. Pr., 2004).

[81] T. Watanabe, J. J. Riley, and K. Nagata, "Effects of stable stratification on turbulent/nonturbulent interfaces in turbulent mixing layers," Phys. Rev. Fluids **1**, 044301 (2016).

[82] M. Zecchetto and C. B. da Silva, "Universality of small-scale motions within the turbulent/non-turbulent interface layer," J. Fluid Mech. **916** (2021).

[83] R. Jahanbakhshi, "Mechanisms of entrainment in a turbulent boundary layer," Phys. Fluids **33**, 035105 (2021).

[84] Y. Long, J. Wang, and C. Pan, "Universal modulations of large-scale motions on entrainment of turbulent boundary layers," J. Fluid Mech. **941**, A68 (2022).

[85] S. Li, Y. Long, and J. Wang, "Turbulent/non-turbulent interface for laminar boundary flow over a wall-mounted fence," Phys. Fluids **34** (2022).

[86] Y. Long, J. Wang, and J. Wang, ""turbulent/non-turbulent interface" in a low-Reynolds-number transitional boundary layer over a multi-element airfoil," Phys. Fluids **34** (2022).

[87] Y. Long, J. Wang, and C. Pan, "The influence of roughness-element-spacing on turbulent entrainment over spanwise heterogeneous roughness," Phys. Fluids **35** (2023).

[88] J. R. Khan and S. Rao, "Properties of the turbulent/non-turbulent layer of a turbulent Boussinesq plume: A study using direct numerical simulation," Phys. Fluids **35**, 055140 (2023).

[89] D. Krug, M. Holzner, B. Lüthi, M. Wolf, W. Kinzelbach, and A. Tsinober, "The turbulent/non-turbulent interface in an inclined dense gravity current," J. Fluid Mech. **765**, 303 (2015).

[90] T. Watanabe, J. J. Riley, and K. Nagata, "Turbulent entrainment across turbulent-nonturbulent interfaces in stably stratified mixing layers," Phys. Rev. Fluids **2**, 104803 (2017).

[91] D. Krug, M. Holzner, I. Marusic, and M. van Reeuwijk, "Fractal scaling of the turbulence interface in gravity currents," J. Fluid Mech. **820** (2017).

[92] T. Katagiri, T. Watanabe, and K. Nagata, "Statistical properties of a model of a turbulent patch arising from a breaking internal wave," Phys. Fluids **33** (2021).

[93] M. M. Neamtu-Halic, J.-P. Mollicone, M. van Reeuwijk, and M. Holzner, "Role of vortical structures for enstrophy and scalar transport in flows with and without stable stratifica-

tion," J. Turbulence **22**, 393 (2021).

[94]M. Boetti, M. van Reeuwijk, and A. Liberzon, "Potential-enstrophy lengthscale for the turbulent/nonturbulent interface in stratified flow," Phys. Rev. Fluids **6**, 114803 (2021).

[95]M. Boetti and L. Verso, "Force on inertial particles crossing a two layer stratified turbulent/non-turbulent interface," Int. J. Multiphase Flow **154**, 104153 (2022).

[96]M. Boetti, "Pair dispersion of inertial particles crossing stably stratified turbulent/non-turbulent interfaces," Int. J. Multiphase Flow **166**, 104502 (2023).

[97]B. Pei and B. Bai, "Species transport in a variable-density turbulent mixing layer considering stratified instability," Phys. Fluids **35** (2023).

[98]K. C. Kim and R. J. Adrian, "Very large-scale motion in the outer layer," Phys. Fluids **11**, 417 (1999).

[99]D. Zhang, J. Tan, and X. Yao, "Direct numerical simulation of spatially developing highly compressible mixing layer: Structural evolution and turbulent statistics," Phys. Fluids **31**, 036102 (2019).

[100]P. L. O ' Neill, D. Nicolaides, D. Honnery, and J. Soria, "Autocorrelation functions and the determination of integral length with reference to experimental and numerical data," in *15th Australasian Fluid Mechanics Conference*, Vol. 1 (University of Sydney, Sydney, NSW, Australia, 2004) pp. 1–4.

[101]O. Praud, A. M. Fincham, and J. Sommeria, "Decaying grid turbulence in a strongly stratified fluid," J. Fluid Mech. **522**, 1 (2005).

[102]Y. Zheng, K. Nagata, and T. Watanabe, "Turbulent characteristics and energy transfer in the far field of active-grid turbulence," Phys. Fluids **33**, 115119 (2021).

[103]D. J. Tritton, *Physical Fluid Dynamics* (Springer Science & Business Media, 2012).

[104]A. J. Puga and J. C. LaRue, "Normalized dissipation rate in a moderate Taylor Reynolds number flow," J. Fluid Mech. **818**, 184 (2017).

[105]J. J. Riley and E. Lindborg, "Stratified turbulence: A possible interpretation of some geophysical turbulence measurements," J. Atmos. Sci. **65**, 2416 (2008).

[106]G. Brethouwer, P. Billant, E. Lindborg, and J.-M. Chomaz, "Scaling analysis and simulation of strongly stratified turbulent flows," J. Fluid Mech. **585**, 343 (2007).

[107]M. Breda and O. R. H. Buxton, "Influence of coherent structures on the evolution of an axisymmetric turbulent jet," Phys. Fluids **30**, 035109 (2018).

[108] T. R. Osborn, “Estimates of the local rate of vertical diffusion from dissipation measurements,” J. Phys. Oceanogr. **10**, 83 (1980).

[109] S. S. Zilitinkevich, T. Elperin, N. Kleeorin, I. Rogachevskii, I. Esau, T. Mauritsen, and M. W. Miles, “Turbulence energetics in stably stratified geophysical flows: Strong and weak mixing regimes,” QQ. J. R. Meteorol. Soc. **134**, 793 (2008).

[110] L. H. Shih, J. R. Koseff, G. N. Ivey, and J. H. Ferziger, “Parameterization of turbulent fluxes and scales using homogeneous sheared stably stratified turbulence simulations,” J. Fluid Mech. **525**, 193 (2005).

[111] P. Monti, G. Querzoli, A. Cenedese, and S. Piccinini, “Mixing properties of a stably stratified parallel shear layer,” Phys. Fluids **19**, 085104 (2007).

[112] M. Lee and R. D. Moser, “Spectral analysis of the budget equation in turbulent channel flows at high Reynolds number,” J. Fluid Mech. **860**, 886 (2019).

[113] T. B. Nickels, I. Marusic, S. Hafez, and M. S. Chong, “Evidence of the k^{-1} law in a high-Reynolds-number turbulent boundary layer,” Phys. Rev. Lett. **95**, 074501 (2005).